

# Mass Models and Sunyaev-Zeldovich Effect Predictions for a Flux Limited Sample of 22 Nearby X-Ray Clusters

Brian S. Mason<sup>1</sup> and Steven T. Myers<sup>2</sup>

*University of Pennsylvania*  
209 S. 33rd St. Philadelphia, PA 19104-6396

## ABSTRACT

We define a 90% complete, volume-limited sample of 31  $z < 0.1$  x-ray clusters and present a systematic analysis of public ROSAT PSPC data on 22 of these objects. Our efforts are undertaken in support of the Penn/OVRO SZE survey, and to this end we present predictions for the inverse Compton optical depth towards all 22 of these clusters. We have performed detailed Monte Carlo simulations to understand the effects of the cluster profile uncertainties on the SZE predictions given the OVRO 5.5-meter telescope beam and switching patterns. We also present a similar analysis for the near-future ACBAR experiment. For most of the clusters in the sample we find less than a 5% uncertainty in the SZE predictions due to an imperfect knowledge of the profile. A comparison of different cooling flow modeling strategies shows that our results are robust with respect to this. The profile uncertainties are then one of the least significant components of our error budget for SZE-based distance measurements. The density models which result from this analysis also yield baryonic masses and, under the assumption of hydrostatic equilibrium, total masses and baryon mass fractions. Our Monte Carlo profile analysis indicates that the baryon masses within  $1 h_{100}^{-1}$  Mpc for these clusters are accurate to better than  $\sim 5\%$  and unaffected by realistic PSPC systematics. In the sample as a whole, we find a mean gas mass fraction of  $(7.02 \pm 0.28) h_{100}^{-3/2} \times 10^{-2}$  internal to  $R_{500} \sim 1 h_{100}^{-1}$  Mpc. This is in agreement with previous x-ray cluster analyses, which indicate an overabundance of baryons relative to the prediction of Big Bang Nucleosynthesis for an  $\Omega_M = 1$  universe. Our analysis of the x-ray spectra confirms a previous claim of an excess absorbing column density towards A478, but we do not find evidence for anomalous column densities in the other 21 clusters. We also find some indications of an excess of soft counts in the ROSAT PSPC data.

A measurement of  $H_o$  using these models and OVRO SZE determinations will be presented in a second paper.

*Subject headings:* galaxies — clusters ; cosmology — distance scale ; cosmology — large scale structure of the universe

---

<sup>1</sup>Current Address: California Institute of Technology, 105-24, Pasadena, CA 91125

<sup>2</sup>Current Address: NRAO, Socorro, NM 87801

## 1. Introduction

The discovery (Giacconi et al. 1972) that many galaxy clusters are also strong sources of x-rays opened a new window on cosmology which has proved fruitful for nearly three decades. Subsequent investigations (e.g., Mitchell et al. 1976; Bahcall & Sarazin 1977) determined that this emission originates in a hot ( $kT_e \sim 7$  keV) thermal plasma with electron number densities of  $\sim$  a few  $\times 10^{-3}$  cm $^{-3}$ . Since the sound-crossing time for pressure waves in this plasma is less than the Hubble time, the plasma can be assumed to accurately trace the cluster gravitational potential. Cluster virial masses obtained in this manner, in conjunction with intracluster medium (ICM) models derived from Einstein and ROSAT observations, have shown an overdensity of baryons relative to the expectation for an  $\Omega_M = 1$ , Big Bang Nucleosynthesis universe (White et al. 1993; White & Fabian 1995; Mohr et al. 1999), thus providing a powerful challenge to the cosmological orthodoxy.

The inverse Compton scattering of Cosmic Microwave Background (CMB) photons—known as the Sunyaev-Zeldovich Effect (SZE)—provides another direct probe of the ICM. As first indicated by Cavaliere et al. (1979), the combination of x-ray and SZE measurements on a given cluster yield a *direct* measurement of the distance to the cluster. If the thermal SZE decrement predicted by the x-ray data under the assumption  $h = 1$  is  $\Delta T_{pred}$ , and the observed decrement is  $\Delta T_{obs}$ , then  $h$  is given by

$$h = \left( \frac{\Delta T_{pred}}{\Delta T_{obs}} \right)^2. \quad (1)$$

Such a calculation requires knowledge of the structure of the cluster along the line of sight; since the x-ray data do not directly provide such information, the clusters are typically assumed to be spherically symmetric. It then becomes important to select clusters from an orientation-unbiased sample. Since the error in  $H_o$  is twice the error in  $\Delta T_{pred}$ , it is also important to accurately understand the statistical and systematic uncertainties inherent in the x-ray models.

The objective of the Penn/OVRO SZE survey is to determine  $H_o$  from observations of the SZE in an x-ray flux-limited sample of nearby clusters. The OVRO 5.5-meter telescope is an ideal instrument for this purpose. At 32 GHz, this telescope has a primary beam of  $7'.35$  (FWHM) and a dual-horn switching angle of  $22'.16$ . At the mean redshift of our sample, these correspond to  $425 h^{-1}$  kpc and  $1.25 h^{-1}$  Mpc, respectively. Since the gas in clusters is distributed on a scale  $r_{core} \sim 200 h^{-1}$  kpc, and most of the gas is contained within the inner  $\sim 1 h^{-1}$  Mpc, the 5.5-meter main beam samples an astrophysically relevant scale while the switching only removes 5 – 10% of the signal. The first results from this survey were reported in Myers et al. (1997): with SZE measurements of four clusters (Coma, Abell 478, Abell 2142, and Abell 2256) and x-ray models from the literature, Myers et al. find  $H_o = 54 \pm 14$  km s $^{-1}$  Mpc $^{-1}$ . The accuracy of these results is limited primarily by the x-ray models.

With this in mind, we have undertaken to expand the sample of Myers et al. and, using public x-ray data, construct high-quality x-ray models and rigorously evaluate their reliability, taking into

account the specific observing strategy employed by our instrument. The spatial resolution and large field of view of the ROSAT PSPC make it ideal for our purposes. While the PSPC does not have the energy or spatial resolution of Chandra or XMM, it has a larger field of view than any instrument on either of these observatories and so imaging analyses of extended objects based on ROSAT data will continue to be relevant for the foreseeable future.

The density models which result from our analysis will also be useful for near-future experiments capable of measuring the SZ distortion resulting from the bulk motion of the cluster gas. To this end we present predictions for the beam-averaged optical depth for the near-future ACBAR experiment, a sensitive bolometric receiver which will begin taking observations in Antarctica early in 2001. This instrument has four frequency channels between 150 GHz and 345 GHz, with matched  $4'$  beams, and will be sensitive to both the thermal and kinematic SZ effects.

In the following section, we first present a brief summary of ICM models (§ 2), along with the formalism associated with these models to describe bremsstrahlung emission and the SZE. § 3 describes our expanded cluster sample, and § 4 the details of the x-ray data analysis, our Monte Carlo error analysis, and the error budget. In this section and the following one, we pay special attention to the effects of central cooling flow emission on our profile models. We present our results in § 5, including mass models and a quantitative assessment of the uncertainties in the SZE predictions, as well as total masses and baryon mass fractions derived under the assumption of hydrostatic equilibrium. We discuss our results and conclude in § 6. Throughout we use  $H_o = 100 h^{-1} \text{km/sec/Mpc}$  and  $q_o = \frac{1}{2}$  unless otherwise specified; we will comment on the impact that assuming other cosmologies has on our results in § 6.

We will report an improved measurement of  $H_o$  using the observations of Myers et al. and Herbig et al. (1995) plus recent observations of Abell 399 in a second paper (paper II). This measurement relies upon the density models we present in this paper, as well as improved electron temperatures from the literature. The consequences of this x-ray analysis in the context of our measurement of  $H_o$  will also be discussed in paper II.

## 2. Models of the Intra-Cluster Medium

One model for the cluster gas which has enjoyed great phenomenological success is the *isothermal beta model* (Cavaliere & Fusco-Femiano 1976). In this case, the gas is assumed to be isothermal, and the electrons distributed according to

$$n_e(r) = n_{eo} \left(1 + r^2/R_0^2\right)^{-3\beta/2}. \quad (2)$$

Here  $n_{eo}$  is the central electron number density,  $r$  is the spherical metric radius, and  $R_0$  is a characteristic scale. The properties of this model are well-known and extensively tabulated in the literature. We have assumed that the ICM is spherically symmetric. While this is not generally the case for individual clusters, it should be a good description on average for an orientation-unbiased

sample (§ 3).

One generalization of the isothermal beta model which has some support both observationally (e.g. Hughes et al. 1988b) and theoretically (e.g. Navarro et al. 1997) is the hybrid isothermal/adiabatic model. In paper II we will study the effects of these models on the SZE, but since the ROSAT data are not sensitive to temperature gradients in the outer parts of the cluster, we will assume an isothermal ICM for the remainder of this analysis. Some authors (e.g. Gunn & Thomas 1996; Holzapfel et al. 1997; Daisuke et al. 1999) have studied the possibility of a multi-phase ICM. In § 4.2 we will present some preliminary indications of cool ICM phases we have found in our analysis. It is, however, difficult to disentangle the effects of these phases from ROSAT calibration uncertainties. We will assess the impact of the observed effect in § 4.2, but until better data from future missions is capable of accurately constraining ICM phase models, we will adhere to the single-phase model.

## 2.1. Thermal Bremsstrahlung

The bolometric luminosity due to bremsstrahlung emission from an ionized thermal plasma of electrons and protons is (Rybicki & Lightman 1979)

$$L = W \times \int_{ICM} n_e n_p T_e^{1/2} \bar{g}(T_e) dV, \quad (3)$$

where

$$W = \left( \frac{2\pi k_B}{3m_e} \right)^{1/2} \times \frac{2^5 \pi e^6}{3hm_e c^3}, \quad (4)$$

$n_e$  is the electron number density,  $n_p$  is the proton number density,  $k_B$  is Boltzmann's constant,  $T_e$  is the local temperature of the plasma, and  $\bar{g}(T_e)$  is the thermally averaged Gaunt factor. For a plasma with the cosmic helium mass fraction  $Y = 0.24$  and metal abundances of 30% solar,  $n_p/n_e = 0.862$ ; this is the value we adopt. This corresponds to a baryonic mass per electron of  $\mu_e = 1.146$  and an overall mean molecular mass (in units of the proton mass)  $\mu = 0.592$ ; these calculations assume the solar abundances of Anders & Grevesse (1989).

For an isothermal plasma, the bolometric flux observed at a redshift  $z$  is

$$S = \frac{W \bar{g}(T_e) T_e^{1/2}}{4\pi D_L^2(z)} \times \int n_e n_p dV. \quad (5)$$

where  $D_L$  is the luminosity distance (Weinberg 1972)

$$D_L = 6000 h^{-1} [(1+z) - \sqrt{1+z}] \text{ Mpc} \quad (6)$$

(for  $q_0 = 1/2$ ). The integral on the right hand side is the Emission Measure (EM):

$$EM = \int n_e n_p dV. \quad (7)$$

For the beta model, the EM over all space reduces to

$$EM = \frac{n_p}{n_e} \pi^{\frac{3}{2}} r_o^3 n_{eo}^2 \frac{\Gamma(3\beta - 3/2)}{\Gamma(3\beta)} \quad (8)$$

If we know the form of the electron density profile ( $\theta_o, \beta$ ), the cluster temperature  $T_e$ , the redshift, and the bolometric flux, we may determine the normalization of the density profile:

$$n_{eo} = \sqrt{\frac{n_e}{n_p} \frac{4}{\pi^{1/2}} \frac{\Gamma(3\beta)}{\Gamma(3\beta - \frac{3}{2})} \frac{1}{\theta_o^3} \frac{(1+z)^6}{D_L} \frac{S}{W\bar{g}(T_e) T_e^{1/2}}}. \quad (9)$$

Here we have used the fact that  $D_L = D_A \times (1+z)^2$ .

In practice the x-ray spectrum is observed over a finite bandpass with a finite aperture, and is modified by photoelectric absorption due to the intervening intra-Galactic medium. We account for this by modeling the spectrum with XSPEC, NASA GSFC's standard x-ray spectral analysis program. XSPEC reports the normalization of the spectrum (a quantity analogous to  $S$  in the foregoing discussion) through the parameter  $K$ , defined as

$$K = \frac{10^{-14}}{4\pi D_L^2} \int n_e n_p dV. \quad (10)$$

Here all distances are in cm. The EM in the annulus between  $\theta_1$  and  $\theta_2$  is

$$EM(\theta_1, \theta_2) = \frac{n_p}{n_e} n_{eo}^2 D_A^3 \theta_o^3 \sqrt{\pi} \frac{\Gamma(3\beta - 1/2)}{\Gamma(3\beta)} \times \frac{2\pi}{3(2\beta - 1)} (C(\theta_1) - C(\theta_2)) \quad (11)$$

where

$$C(\theta) = \left[ 1 + \left( \frac{\theta}{\theta_o} \right)^2 \right]^{-3\beta+3/2}. \quad (12)$$

The central density is then

$$n_{eo} = 4.160 \times 10^{-3} \text{ cm}^{-3} h^{1/2} \times \left[ \frac{n_e/n_p}{1.16} (\beta - 1/2) \frac{\text{arccmin}^3}{\theta_o^3} \frac{(1+z)^6}{1+z-\sqrt{1+z}} \frac{\Gamma(3\beta)}{\Gamma(3\beta - 1/2)} \frac{K/10^{-2}}{C(\theta_1) - C(\theta_2)} \right]^{\frac{1}{2}}. \quad (13)$$

Note that Eq. 6 used in deriving this equation assumed  $q_o = \frac{1}{2}$ ; for  $z = 0.1$  this causes at most a  $\pm 1\%$  error in  $n_{eo}$  for  $\Delta q_o = \pm \frac{1}{2}$ . This is the expression we use to determine the normalization of the cluster density profiles.

## 2.2. The Sunyaev-Zeldovich Effect

Sunyaev & Zeldovich (1980) show that the fractional change in intensity due to the inverse Compton scattering of CMB photons by a thermal plasma with a velocity  $v_r$  along the line of sight is

$$\frac{\Delta I_\nu}{I_\nu} = \tau \frac{x e^x}{e^x - 1} \times \left( \frac{kT_e}{m_e c^2} f(x) + \frac{v_r}{c} + \Theta(T_e, v_r) \right), \quad (14)$$

where  $T_e$  is the temperature of the plasma,  $\tau$  is the optical depth for inverse Compton scattering

$$\tau = \sigma_T \int n_e(z) dz, \quad (15)$$

$x$  is the dimensionless frequency

$$x = \frac{h\nu}{kT_{cmb}}, \quad (16)$$

and

$$f(x) = x \coth(x/2) - 4. \quad (17)$$

$\Theta(T_e, v_r)$  is a relativistic correction (Rephaeli 1995; Challinor & Lasenby 1998; Sazonov & Sunyaev 1998), which generally has a magnitude of a few percent that of the leading term for  $T_e \lesssim 10$  keV. In Eq. 15,  $\sigma_T$  is the Thompson scattering cross section ( $6.65 \times 10^{-25}$  cm<sup>2</sup>) and the integral is along the line of sight. Since the ROSAT PSPC data are not sensitive to temperature gradients, they are capable of directly constraining the cluster density profiles. For this reason we express our SZE analysis in terms of the inverse Compton optical depth. Note that this also renders the results we present here independent of the relativistic correction  $\Theta(T_e, v_r)$ , although this will have to be taken into account when relating the  $\tau$  values we present to observed intensity decrements.

A radio telescope will measure the intensity decrement convolved with the instrument beam pattern. It is then convenient to consider the quantity

$$\tau_{beam} = \frac{1}{\Omega_{Beam}} \int d\Omega \tau(\hat{\Omega}) R_N(\hat{\Omega}) \quad (18)$$

where  $R_N(\hat{\Omega})$  is the telescope beam normalized to unity at the maximum.  $R_N$  is typically well described by a Gaussian:

$$R_N(\hat{\Omega}) = e^{-\theta^2/2\sigma^2}. \quad (19)$$

For the OVRO 5.5-meter telescope we have  $\sigma_{5.5-m} = 3'.12 \pm 0.11$  (Leitch 1998), and for ACBAR,  $\sigma_{ACBAR} = 1'.7$ . The 5.5-meter telescope also switches by  $22'.16$  in azimuth to remove atmosphere and ground emission. We then define

$$R_{sw}(\hat{\Omega}) = R_N(\hat{\Omega}) - R_N(\hat{\Omega} - \delta\hat{\Omega}) \quad (20)$$

where  $\delta\hat{\Omega}$  is the switching vector which, at a given Hour Angle, corresponding to a  $22'.16$  offset in azimuth. Since our analysis assumes spherical symmetry for the clusters, we will always compute this quantity at transit. The equivalent quantity to  $\tau_{beam}$  then is

$$\tau_{sw} = \frac{1}{\Omega_{Beam}} \int d\Omega \tau(\hat{\Omega}) R_{sw}(\hat{\Omega}). \quad (21)$$

In terms of these objects, the equivalent temperature decrement which a single-dish telescope will see for an isothermal cluster is

$$\Delta T_{eq} = T_{cmb} \frac{x^2 e^x}{(e^x - 1)^2} f(x) \frac{kT_e}{m_e c^2} \tau_{sw}. \quad (22)$$

For more details on this formalism, see Myers et al. (1997) and Mason (1999).

### 3. The Sample

Due to the assumption of spherical symmetry necessary to employ the Sunyaev-Zeldovich effect as a distance measure, it is vital to measure the SZE in an unbiased sample. An x-ray selected, x-ray flux limited sample satisfies this criterion. The first steps in this direction were taken by Myers et al. (1997) who used the sample of Edge et al. (1990) to define an x-ray flux limited sample of 11 clusters with  $z < 0.1$ ,  $f_x > 3.11 \times 10^{-11} \text{ erg cm}^{-2} \text{ s}^{-1}$  (2-10 keV), galactic latitudes  $|b| > 20^\circ$ , and declinations  $\delta > -23^\circ$ . We improve upon this by defining a larger sample. This has two advantages. First, it will allow the (random) noise caused by departures from spherical symmetry to be reduced in the sample average. Second, it will allow many possible systematic affects to be identified by dividing the sample into several sub-samples by, *e.g.*, morphology, optical richness, or x-ray spectral characteristics.

As our parent sample we choose the XBAC catalog of Ebeling et al. (1996). Ebeling et al. have analyzed the data of the Rosat All Sky Survey (RASS) to obtain a sample of 242 Abell clusters complete at the 95% level down to a flux limit of  $5.0 \times 10^{-12} \text{ erg cm}^{-2} \text{ s}^{-1}$  in the 0.1–2.4 keV band. If we conservatively adopt a flux cutoff of twice this ( $1.0 \times 10^{-11} \text{ erg cm}^{-2} \text{ s}^{-1}$ ) and impose the luminosity cutoff ( $D_L(z = 0.1) = 291.52 h^{-1} \text{ Mpc}$  for  $q = 1/2$ ) corresponding to a volume complete sample out to  $z = 0.1$ , we find 31 clusters in the XBAC catalog that meet these criteria. These are listed in Table 1.

Since the XBAC catalog ultimately uses the list of Abell clusters as a parent sample, we must employ some caution in assessing the completeness of our sample. By comparing the overlap regions of the Abell (Abell 1958) and ACO (Abell et al. 1989) catalogs, Scaramella et al. (1991) find that Abell missed 29% of the Richness class 1 or greater clusters which were in ACO; most of these are  $R = 1$  objects. These results are consistent with the results of Van Haarlem et al. (1997), who find that 30% of  $R \geq 1$  objects are missed in Monte Carlo simulations with an optical selection algorithm designed to mimic that of Abell and ACO. In most cases, these clusters are missed due to fluctuations in the background galaxy counts, resulting in the misclassification of actual clusters as poorer objects which are then not included in the catalog; since this misclassification preferentially affects the poorer clusters, most of the missed clusters are again likely to be Richness class 1 objects. Our stringent luminosity criterion strongly selects against these poorer objects: only 23% of our 31 cluster sample are  $R \leq 1$ , whereas 67% of the 242 clusters in the XBAC catalog have  $R \leq 1$ . Van Haarlem et al. find that a luminosity cutoff comparable to the one we have imposed, applied after the optical selection, results in a catalog which is free from false detections (although this does not directly address the issue of orientation bias).

Based on these considerations, we estimate our sample to be 90% complete for  $L_o = 1.13 \times 10^{44} h^{-2} \text{ erg s}^{-1}$ ,  $f_o = 1.0 \times 10^{-11} \text{ erg cm}^{-2} \text{ s}^{-1}$ . This corresponds to 3 missed clusters at most. This level of incompleteness will not significantly affect  $H_o$  measurements derived from the sample as a whole. Near-future, fully x-ray selected surveys such as the ESO REFLEX survey will provide an important cross-check on the completeness of this sample.

Source	RA	Dec	$F_x$	$L_x$
A2142	15:58:22.1	+27:13:58.8	61.4	20.74
A2029	15:10:55.0	+05:43:12.0	61.6	15.35
A478	04:13:26.2	+10:27:57.6	39.1	12.95
A1795	13:48:52.3	+26:35:52.8	67.2	11.12
A401	02:58:56.9	+13:34:22.8	42.6	9.88
A2244	17:02:40.1	+34:03:46.8	22.8	9.09
A3667	20:12:23.5	−56:48:46.8	73.1	8.76
A85	00:41:48.7	−09:19:04.8	72.3	8.38
A1651	12:59:24.0	−04:11:20.4	27.1	8.25
A754	09:09:01.4	−09:39:18.0	64.1	8.01
A2597	23:25:16.6	−12:07:26.4	25.9	7.97
A1650	12:58:41.8	−01:45:21.6	25.6	7.81
A3827	22:01:56.6	−59:57:14.4	18.7	7.78
A3112	03:17:56.4	−44:14:16.8	36.4	7.70
A3571	13:47:28.1	−32:51:14.4	109.5	7.36
A1656	12:59:31.9	+27:54:10.8	316.5	7.21
A2256	17:04:02.4	+78:37:55.2	49.0	7.05
A2384	21:52:16.6	−19:36:00.0	18.2	6.82
A780	09:18:06.7	−12:05:56.4	48.4	6.63
A399	02:57:49.7	+13:03:10.8	29.0	6.45
A3558	13:27:57.8	−31:29:16.8	64.6	6.27
A3266	04:31:25.4	−61:25:01.2	48.5	6.15
A4010	23:31:14.2	−36:30:07.2	14.1	5.55
A3921	22:49:59.8	−64:25:51.6	14.0	5.40
A3158	03:42:43.9	−53:38:27.6	35.7	5.31
A2426	22:14:32.4	−10:21:54.0	12.2	5.10
A3695	20:34:46.6	−35:49:48.0	15.1	5.07
A2065	15:22:26.9	+27:42:39.6	22.3	4.95
A2255	17:12:45.1	+64:03:43.2	17.2	4.79
A566	07:04:22.3	+63:16:30.0	11.3	4.62
A3911	22:46:20.9	−52:43:30.0	11.8	4.61

Table 1: SZE cluster XBAC subsample. Columns are: Right Ascension and Declination (J2000),  $F_x$ ,  $10^{-12}$  erg cm $^{-2}$  s $^{-1}$ , 0.1 – 2.4 keV ;  $L_x$ ,  $10^{44}$  erg s $^{-1}$ ,  $h = \frac{1}{2}$ . Fluxes and luminosities are as reported by Ebeling et al. and assume  $h = 0.5$ .



In Table 2 we summarize redshift and temperature data from the literature on the 22 clusters with public ROSAT data in our sample. Where available, we use the Markevitch et al. (1998) ASCA temperatures which properly account for cooling flow contamination of the x-ray spectrum. We also list the Hydrogen column densities employed in the spectral analysis (§ 4.2). With the exception of A478 we use the Galactic neutral Hydrogen values of Stark et al. (1992) as interpolated onto the cluster coordinates by PIMMS/COLDEN. For A478 we use the column density resulting from our x-ray spectral analysis; this is discussed further in § 4.2. While the 22 clusters in Table 2 are not strictly speaking a flux-limited sample, we note that ROSAT targets are preferentially high-luminosity clusters (as opposed to morphologically selected clusters) and thus the 22 cluster sub-sample is likely to be free from orientation effects also. Three of the 9 missed clusters have non-public ROSAT observations (A4010, A2426, and A3695) and one (A2384) has HRI observations only; these four observations plus future XMM observations for which we will propose will help fill out the sample.

Cluster	$T_e$ keV	$N_H$ $10^{20} \text{cm}^{-2}$	$z$
A85	$6.9 \pm 0.4$	3.44	0.0518
A399	$7.0 \pm 0.4$	10.9	0.0715
A401	$8.0 \pm 0.4$	10.5	0.0748
A478	$8.4^{+0.8}_{-1.4}$	21.1*	0.0900
A754	$9.5^{+0.7}_{-0.4}$	4.36	0.0528
A780	$4.3 \pm 0.4$	4.94	0.0522
A1651	$6.1 \pm 0.4$	1.81	0.0825
A1656	$9.1 \pm 0.7^A$	0.92	0.0232
A1795	$7.8 \pm 1.0$	1.19	0.0616
A2029	$9.1 \pm 1.0$	3.06	0.0767
A2142	$9.7^{+1.5}_{-1.1}$	4.20	0.0899
A2244	$7.1^{+5.0}_{-2.2}^B$	2.13	0.0980
A2255	$7.3^{+3.3}_{-1.6}^B$	2.59	0.0800
A2256	$6.6 \pm 0.4$	4.10	0.0601
A2597	$4.4^{+0.4}_{-0.7}$	2.49	0.0852
A3112	$5.3^{+0.7}_{-1.0}$	2.60	0.0703 <sup>C</sup>
A3158	$5.5 \pm 0.6^B$	1.35	0.0590 <sup>C</sup>
A3266	$8.0 \pm 0.5$	1.60	0.0594 <sup>C</sup>
A3558	$5.5 \pm 0.4$	3.88	0.0482 <sup>C</sup>
A3571	$6.9 \pm 0.2$	3.70	0.0397 <sup>D</sup>
A3667	$7.0 \pm 0.6$	4.76	0.0552 <sup>E</sup>
A3921	$6.6 \pm 1.6^F$	2.95	0.0960 <sup>G</sup>

\* ROSAT value; Stark et al. gives 14.8

<sup>A</sup> Hughes et al. (1988a)

<sup>B</sup> David et al. (1993)

<sup>C</sup> Abell et al. (1989)

<sup>D</sup> Vettolani et al. (1990)

<sup>E</sup> Sodre et al. (1992)

<sup>F</sup> Ebeling et al. (1996) with our estimated error.

<sup>G</sup> Dalton et al. (1994)

Table 2: Electron temperatures are from Markevitch et al. (1998) except as noted; redshifts are from Struble & Rood (1991) except as noted. All errors are 90% ( $\sim 1.65 - \sigma$ ) confidence limits.

#### 4. Data Analysis

We searched the public ROSAT data archive for observations of the 31 clusters in Table 1 and found a total of 44 observations on 22 clusters. These data form the basis for our analysis; the data sets are listed in Table 3, along with the ROSAT sequence ID, exposure time, approximate pointing offset from the cluster center, and date of the ROSAT observation. We assign an observation tag (e.g., A754d) to each observation for convenience. After the date we indicate the detector used for each observation: PSPC B (B), PSPC B/High gain (BH), or PSPC C (C). We will use the redundancy of the data to search for possible ROSAT calibration errors.

For each observation of a cluster with a single instrument (PSPC B and BH— there were no multiple observations with the PSPC C), all individual pointings were mosaicked using the ESAS software described below to form a single count rate image for the cluster. These data form the basis for our highest signal-to-noise analyses where available. These mosaicked observations are referred to by the tags BM and BHM; a catalog of the mosaics is presented in Table 4. After this step, the mosaics are analyzed in the same fashion as the single-pointing observations.

In order to clean the data and correct for telescope vignetting, as well as for the mosaicking, we used the Extended Source Analysis Software (ESAS); see Snowden et al. (1994) for more details on this package. Table 5 shows the energy channel definitions employed by this software. While in principle the cluster luminosity may be inferred by observations over a single band (e.g., by co-adding R4–R7), we chose to analyze each band separately. This allows us to check the suitability of our x-ray models more carefully. All data with Master Veto count rates greater than 170 counts per second were rejected. The end product of the ESAS analysis are 512 x 512 pixel maps (each pixel 14".947 on a side) of the cleaned, vignetting corrected count rate, the exposure, and the raw counts. ESAS also provides a map of the background model used in cleaning the data. These products are provided for each of the seven analysis channels, and also for the co-added R4–R7 channel which we use for the profile analysis.

Point source masks were derived using ESAS’s DETECT algorithm, which employs a variable

detection aperture to account for the change in the ROSAT point-spread function across the detector face. We masked all sources detected with greater than 99% confidence in the 0.5 – 2.0 keV band having total count rates greater than  $5 \times 10^{-3}$  counts per second. This is potentially important, since the variability of the point spread function and the detector vignetting are likely to bias point source masks created “by eye”. Using the exposure maps calculated by ESAS, all regions with exposures less than 30% of the maximum are also masked; this removes data for which the vignetting correction is more than a factor of  $\sim 3$ . Typically  $\sim 10\%$  of the pixels are masked by this step, primarily those shadowed by the PSPC window support structure. These masks were employed to exclude data in the subsequent profile and spectral analysis.

Cluster	Sequence ID	Observation Tag	Exposure (sec)	Offset (arcmin)	Observation Date
<b>A85</b>	rp800250N00	a85a	10238	4.74	01jul92 (B)
	rp800174A00	a85b	2187	5.20	20dec91 (B)
	rp800174A01	a85c	3458	5.20	11jun92 (B)
<b>A401</b>	rp800182N00	a401a	6735	0.22	23jan92 (B)
<i>(incl. A399)</i>	rp800235N00	a401b	7457	0.22	30jul92 (B)
<b>A478</b>	rp800193N00	a478a	21969	0.4	31aug91 (BH)
<b>a754</b>	rp800550N00	a754a	8156	12.13	06nov93 (B)
	rp600451N00	a754b	13495	22.34	03nov92 (B)
	rp800160N00	a754c	2266	12.13	19nov91 (B)
	rp800232N00	a754d	6358	12.13	10nov92 (B)
<b>A780</b>	rp800318n00	a780a	18398	12.00	08nov92 (B)
<b>A1651</b>	wp800353	a1651a	7435	3.41	18jul92 (B)
<b>A1656</b>	rp800009n00	a1656a	20345	33.04	16jun91 (BH)
	rp800006n00	a1656b	21545	9.98	16jun91 (BH)
	rp800005n00	a1656c	21140	2.23	17jun91 (BH)
	rp800013n00	a1656d	21428	15.85	18jun91 (BH)
<b>A1795</b>	rp700284N00	a1795a	2025	13.84	30jun91 (BH)
	rp700145A01	a1795b	1909	13.84	06jan92 (B)
	rp700145A00	a1795c	18205	13.84	01jul91 (BH)
	rp800105N00	a1795d	36273	0.58	04jan92 (B)
	rp80055N00	a1795e	25803	1.67	09jul91 (BH)
<b>A2029</b>	rp800161N00	a2029a	3151	1.12	24jan92 (B)
	rp800249N00	a2029b	12542	0.32	10aug92 (B)
<b>A2142</b>	rp800415N00	a2142a	19208	15.78	21aug92 (B)
	rp150084N00	a2142c	7734	0.46	20jul90 (C)
	wp800096	a2142d	6192	0.46	25aug92 (B)
	rp800551N00	a2142e	6090	0.46	23jul93 (B)
	rp800233N00	a2142f	4939	0.46	26aug92 (B)
<b>A2244</b>	rp800265N00	a2244a	2963	1.82	21sep92 (B)
<b>A2255</b>	rp800512n00	a2255a	14555	1.64	24aug93 (B)
<b>A2256</b>	rp100110N00	a2256a	17032	0.18	17jun90 (C)
	rp800163N00	a2256b	10681	14.51	25nov91 (B)
	rp800340N00	a2256e	9422	22.59	25jul92 (B)
	rp800341N00	a2256f	10473	16.54	23jul92 (B)
	rp800162A00	a2256g	4246	13.35	15oct91 (B)
	rp800162A01	a2256h	4747	13.35	15mar92 (B)
	rp800339N00	a2256i	4978	13.35	22jul92 (B)
<b>A2597</b>	rp80012N00	a2597a	7163	1.12	27nov91 (B)
<b>A3112</b>	rp800302N00	a3112a	7598	4.50	17dec92 (B)
<b>A3158</b>	rp800310n00	a3158a	3020	19.08	26aug92 (B)
<b>A3266</b>	rp800552N00	a3266a	13547	2.14	19aug93 (B)
<b>A3558</b>	rp800076n00	a3558a	29490	1.48	17jul91 (BH)
<b>A3571</b>	rp800287n00	a3571a	6062	12.08	12aug92 (B)
<b>A3667</b>	rp800234n00	a3667a	12550	0.26	09oct92 (B)
<b>A3921</b>	rp800378n00	a3921c	11997	1.19	15nov92 (B)

Table 3: ROSAT PSPC observations of clusters in our sample. Shown are the cluster name, the ROSAT Sequence ID, the observation tag we assign to the observations, the exposure time in seconds, the offset of the ROSAT pointing center from the cluster center, and the date of the ROSAT observation.

Mosaic	Pointings
A2142BM	A2142A,E,F
A2256BM	A2256B,E-I
A85BM	A85A-C
A401BM	A401A,B
A754BM	A754A-D
A2029BM	A2029A,B
A1795BHM	A1795A,C,E

Table 4: A catalog of the mosaics used in the spectral analysis. We show the mosaic tag that we use for reference, and the individual observations composing each mosaic.

Band	Energy	Centroid
Name	(keV)	(keV)
R1	0.11 – 0.284	0.197
R2	0.14 – 0.284	0.212
R3	0.20 – 0.83	—
R4	0.44 – 1.01	0.725
R5	0.56 – 1.21	0.850
R6	0.73 – 1.56	1.140
R7	1.05 – 2.04	1.540

Table 5: Snowden PSPC energy band definitions, along with their approximate centroids. Since band 3 straddles an absorption edge due to carbon in the PSPC window, it is not significant to designate a centroid for this band. This band is not used in any subsequent analysis.

#### 4.1. Profile Analysis

We used the composite R4–R7 count rate image to determine the spatial profile of each cluster. Where mosaicked observations were possible, we used these. The centroid of each image was computed in a circle centered on the visual peak of emission<sup>3</sup>, and an azimuthal profile was constructed with 150 bins out to a radius equivalent to  $1.5h^{-1}$  Mpc or  $50'$ , whichever was less. We find that our profile results are not sensitive to the binning. Error bars were assigned by performing an identical procedure on the co-added R4–R7 raw count images, and assigning the fractional Poisson error for each bin in the raw count profile (based on the total number of counts in that bin) to the corresponding bin in the count-rate profile.

The resulting profile was fit to a beta model surface brightness profile:

$$I(\theta) = I_o \times \left(1 + \frac{\theta^2}{\theta_0^2}\right)^{-3\beta + \frac{1}{2}}. \quad (23)$$

For cooling flow clusters in which a good fit could not be obtained for a beta model, we added a Gaussian component of emission to the profile (see below). In these fits,  $\theta_0$ ,  $\beta$ ,  $I_o$ , and the central intensity and width of the Gaussian were all free parameters. A free constant background term was also included. The best-fit parameter values were obtained using a standard non-linear least-squares code (Press et al. 1992), and the uncertainties in these parameters were determined from our Monte Carlo analysis (§ 4.4.1). In order to protect the assumption of Gaussianity implicitly assumed by the least-squares method, any bins in the profile with fewer than 16 counts total were rejected. This precaution was only necessary for some of the shortest exposures (e.g., A2244a); more typically, all of the bins in the profile had  $\gtrsim 50$  counts.

In § 4.4.1 we will describe the Monte Carlo simulations which we use to establish the confidence intervals for the profile parameters. Note, however, that the Monte Carlo technique assumes at the outset some parametric model for the cluster profile, which is then fit to multiple simulated data

---

<sup>3</sup>The only exception to this was A754, where we varied the center used for the azimuthal average until a good beta model fit could be obtained. The resulting centroid is  $\alpha = 137^\circ.314, \delta = -9^\circ.674$  (J2000). The uncertainty induced by this procedure will be accounted for in our Monte Carlo simulations (§ 4.4.1)

sets. If the chosen profile is simply not appropriate, that fact may not be reflected in the resultant confidence intervals. This issue is especially important for the cooling flow clusters: a single beta model does not typically fit the azimuthal profile of these clusters over the full range of interesting radii, and the fits tend to be strongly driven by the high signal-to-noise data in the cluster core. The literature shows that investigators have developed a number of strategies to model these clusters. For example, Briel & Henry (1996) and Henry & Briel (1996), in modeling Abell 1795 and 2142, exclude the inner  $3' - 5'$  of the profile and fit the outer part to a standard beta model. Mohr et al. (1999) model the cooling flow clusters in their sample as the sum of two beta model profiles in emission, and numerically solve for the underlying density profile.

For the cooling flow clusters in our sample we chose to construct two models for each cluster using methods similar to each of these strategies. This analysis allows us to quantitatively evaluate the impact of our cooling-flow modeling strategy on the scientific results we present. The first method we use is to fit the projected emission profile to a beta model plus a Gaussian component (to represent the central excess of emission over the beta model). Since modeling the central emission is highly uncertain because of the complicated physics in this region, we ignore the fitted excess in constructing density profiles for the subsequent analysis<sup>4</sup>. Our second strategy (similar to that of Briel and Henry) is to excise data out to a radius of  $150 h^{-1}$  kpc in the image and fit a beta model to the remaining data. Note that this method provides a less core-weighted measurement than the former method, and since the SZE tends to be dominated by the emission from the outer parts of the cluster, this is an important diagnostic. The same considerations pertain for the total mass measurement, which depends only upon the derivative of the density profile at some (typically large) radius.

The former (beta plus Gaussian component) models we will refer to as the “primary” models for the cooling flow clusters. In the final analysis all of our baryon models (and therefore baryonic

---

<sup>4</sup>A comparison with Mohr et al. (to be provided in § 6) will show up any systematic errors in the baryonic masses due to this procedure, as these authors retain the central excess and solve for the underlying 3-D profile assuming a single-phase ICM.



masses and SZ predictions) employ the primary models. The models derived from profiles with the central regions excised we identify as “alternate” models. *Since the alternate models will more accurately measure the gradient in the outer regions of the cluster atmosphere, we always use these to measure the total mass in the cooling flow clusters.* In § 5.1 we show that failing to do this will overestimate the total mass by 6% on average. We will also use the alternate baryon models to bracket the uncertainty in our SZE predictions induced by our choice of modeling strategy. In the tables that follow we refer to the primary and alternate models for a given cluster as, e.g., “A85” and “A85.2”.

For all clusters without evidence for a cooling flow, we use a single beta model fit to the profile (both for the baryon model and for the total mass).

Generally we find that the reduced  $\chi^2$  values for the fits are not consistent with unity. Since it is straightforward to obtain robust, qualitatively good fits to the azimuthal profiles given the methods detailed above, we do not quote the  $\chi^2_{\nu}$  values for the fits. Appendix A shows our fits to the cluster radial profiles.

Our results will be summarized in § 5.1.

## 4.2. Spectral Analysis

In order to determine the cluster count rate in a given energy band, it is necessary to separate the contributions of cosmic and residual instrumental backgrounds in the image from that of the cluster. We investigated two methods of accomplishing this. First, we used a traditional approach wherein the background count rate was estimated from an annulus encompassing the region lying between  $35'$  and  $40'$  from the cluster centroid (the “ring” method). Second, we tried extracting the cluster count rates directly from each band by fitting the azimuthal profile of that band to a beta model count rate profile (the “ $\beta$ ” method) with a free constant background. We found the  $\beta$  method to be less sensitive to variable backgrounds and overall somewhat more stable than the ring method; indeed, for the soft bands (R1 and R2) the ring spectra often provide meaningless results. Since the  $\beta$  spectra also correctly interpolate the cluster flux in masked regions and are less sensitive to the details of the point source masking, we used this method in the analysis.

The cluster count rates were extracted from each of the R1, R2, and R4–R7 using this strategy. R3 contains little signal due to a Carbon  $K\alpha$  edge caused by the PSPC window and is not generally supported by EXSAS, so we discard the data from this band. Due to the likelihood of the x-ray spectra being contaminated by extra cool phases in the cluster core, we excised the inner  $150 h^{-1}$  kpc of emission for clusters in which Markevitch et al. (1998) detect a significant central cool component of emission. Our fiducial cut radius is well beyond the cooling radius for most of the clusters in our sample. Peres et al. (1998) obtain a cooling radius ( $r_{cool} = 102_{-27}^{+38} h^{-1}$  kpc) for A1795, one of the strongest cooling-flow clusters in our sample; even for this cluster, there is a margin for error. This relatively extreme excision also insures that our models are sampling the large scales relevant for the SZE and baryonic mass. The fractional uncertainty in each band’s count rate was calculated by adding the Poisson uncertainty (calculated from the equivalent non-vignetting-corrected spectrum) in quadrature with an additional 1.5% uncertainty estimated by inspecting the fits to a few initial data sets. This latter correction was necessary to make  $\chi^2_{\nu} \sim 1$  for fits to these data.

These count rates and uncertainties were converted into .pha files using the FT00L `ascii2pha`

and analyzed with XSPEC. Each spectrum was modeled by one or more Raymond-Smith thermal plasmas with photoelectric absorption as described below. The plasma temperatures and redshifts used in this analysis are those shown in Table 2. We used the standard GSFC response matrices<sup>5</sup> for the PSPC B, PSPC B(H), and PSPC C, rebinned as per the energy channel definitions of Snowden et al. (1994).

In our initial analysis of the spectral data, we allowed the absorbing column density to be a free parameter which we then fit to the R2 and R4–R7 data. The results of this exercise are somewhat discouraging. Out of 22 clusters, 4 (A478,A754, A2256, and A3266) show absorbing column densities higher than the Galactic value, 3 (A401, A2029, and A3158) are consistent or marginally consistent with the Galactic value, and 15 are significantly lower than the Galactic value. While it would be possible for the column densities to be systematically *higher* than the Galactic column density due to extragalactic neutral hydrogen along the line of sight (e.g., associated with the cluster), no effect can make the absorbing column densities systematically *lower* than the Galactic value. Substructure in the Galactic disk, for example, should only cause a scatter in the observed column densities.

The fact that we consistently observe a deficit in the fitted column density relative to the Galactic expectation is equivalent to there being an excess of counts in the soft channels if we consider the Galactic hydrogen column densities, on average, to be reliable. There are two possible explanations for such an effect. One is that in most of the clusters we observe, there is a widespread cool phase. While this is not likely at radii larger than the cooling radius, a variety of astrophysical mechanisms may permit such a situation (see, for example, Gunn & Thomas 1996). In order to diagnose the significance of this, we examined in detail three of the clusters (A85, A1651, and A1656) showing particularly low column densities in our spectral fits. In two of the three cases (A1651 and A1656) fits of comparable quality to the free Hydrogen column density fit are achieved if the gas is assumed to be at  $\sim 0.1$  keV with the column density fixed at the Galactic value; in these cases, the contribution of the cooler phase to the observed flux is  $\sim 5\%$  of the total flux. Since

---

<sup>5</sup>Available at [http://heasarc.gsfc.nasa.gov/docs/rosat/pspc\\_matrices.html](http://heasarc.gsfc.nasa.gov/docs/rosat/pspc_matrices.html)

the cool phases (under the assumption of hydrostatic equilibrium) are highly over-represented in the x-rays, such a phase in itself contributes negligibly to the baryonic mass and hence the SZE. On the other hand, the best-fit flux for the dominant (hot) Raymond-Smith component is reduced by  $\sim 5\%$  for these two clusters; this is comparable to the reduction in de-absorbed flux that we infer for a single-component fit with a free absorbing column density for these clusters.

A more likely possibility is that there is a systematic error in the PSPC calibration. This has recently been suggested by Iwasawa et al. (1999) on the basis of a comparison of the spectral indices inferred from ASCA and ROSAT data on the AGN NGC5548. These authors find that the ROSAT spectral index is significantly steeper than the ASCA spectral index over the same energy range. This is consistent with the excess of soft counts which we observe. Markevitch & Vikhlinin (1997) have noted that ROSAT temperatures are consistently lower than those obtained with ASCA, GINGA, and EINSTEIN; this is also consistent with what we see.

The most significant case of absorption *over* the Galactic value in our sample is A478. For this cluster, the level of absorption is enough to render R1 and R2 effectively useless; nevertheless, we are able to constrain the absorbing column density using only bands R4–R7. If we exclude the central  $150h^{-1}$  kpc of emission and fix the absorbing column density at the Galactic value ( $14.8 \times 10^{20} \text{cm}^{-2}$ ), the best-fit Raymond-Smith model has  $\chi_{\nu}^2 = 17.7$  for 3 D.O.F.; allowing the absorbing column density to be free and fitting for it, we obtain  $21.1 \pm 1.0 \times 10^{20} \text{cm}^{-2}$  with  $\chi_{\nu}^2 = 1.90$  for 2 D.O.F. We also tried modeling the spectrum with two Raymond-Smith components (one at 8.4 keV and one at a range of hotter temperatures) plus Galactic absorption; all of these yielded  $\chi_{\nu}^2$  values *higher* than those given by the single-phase Galactic absorption fits. Our best results are consistent with the result of a single-phase fit to all of the cluster emission (including the cooling flow), which yields an absorbing column density of  $22.5 \pm 0.7 \times 10^{20} \text{cm}^{-2}$  and  $\chi_{\nu}^2 = 3.2$  for 2 D.O.F.; allowing a second, cool phase in this fit yields a lower  $\chi_{\nu}^2$  and a slightly higher column density. The column densities we determine are significantly in excess of the Galactic value. Allen et al. (1993) have measured an absorbing column density of  $24.9_{-0.9}^{+1.2} \times 10^{20} \text{cm}^{-2}$ ; if we adopt the electron temperature they have used in their analysis (6.6 keV) we achieve results consistent with

theirs at the  $1.5\sigma$  level. Note the Allen et al. measurement also uses ROSAT data. For this cluster and this cluster only, we use our best-fit column density ( $21.1 \pm 1.0 \times 10^{20} \text{cm}^{-2}$ ) instead of the Galactic column density. If the Galactic column density is used instead, the cluster luminosity is underestimated by 18%.

In light of the above considerations, we have fixed all of the hydrogen column densities (except for A478) at the Galactic value. Most clusters we model with a single Raymond-Smith component. However, some cluster spectra (A401, A3558, and A3921) were not well described by a single Raymond-Smith component even when the column density was allowed to vary. For these clusters, including a second plasma component at a fiducial temperature of  $T_e = 1 \text{keV}$  improves the fit relative to a single-phase Raymond-Smith model (even with a free Hydrogen column density). In all of these cases,  $\sim 10\%$  of the flux is in the 1 keV component, corresponding to 1 – 2% of the mass for a uniform, isobaric ICM. It is interesting that two of these three clusters (A401 and A3558) are in the early stages of a major merger; the third shows a highly elliptical x-ray morphology.

For all of the clusters, the deabsorbed flux ( $K$ ) of the hot (dominant) Raymond-Smith component is used to determine the baryonic mass (via Eq. 13); we use the uncertainties (68% for one interesting parameter,  $K$ ) determined by the `XSPEC fit` command. For the cases at hand these are comparable to those determined by the `error` command. Due to the possibility of a systematic calibration error in the soft channels, we use only R4–R7 for the spectral fits.

If we use our best fit absorbing column densities for the sample as a whole (excluding A478), the average ratio of the de-absorbed luminosity to the de-absorbed luminosity inferred assuming Galactic absorption is  $0.977 \pm 0.007$ . We take this 2.3% error as indicative of the level of systematic error induced by the calibration error suggested by Iwasawa et al. (1999) and/or cool phases at large radius and include it in our final error budget.

We use the fluxes  $K$  determined by this method together with the cluster density profiles to determine the central density  $n_{eo}$  via Eq. 13.

### 4.3. Notes on Individual Clusters

Since galaxy clusters are not entirely uniform morphologically or spectrally, a few special cases are inevitable in the analysis of large data sets. Here we indicate special measures taken for individual objects. Unless otherwise noted, the  $\chi^2$  values and significance levels are for fits with the absorbing column density fixed at the Galactic value and using bands R4–R7. Note that the clusters requiring additional soft components in the spectral fit were identified as requiring such on the basis of fits *including a free absorbing column density*, although (as indicated above, and except for A478) our final results all assume a column density fixed at Galactic.

- **A85:** The emission from an infalling group of galaxies to the south of the main cluster center was excised from the image prior to the analysis.
- **A399:** A399 and A401 lie within the same field of view separated by some  $37'$ . A401 was excised from the image (out to a radius of  $25'$ ) prior to the analysis.
- **A401:** An excess soft component of emission over the best-fitting Raymond-Smith model is detected at the  $3\sigma$  level. The best fitting single component model has  $\chi^2_\nu = 7.8$ , whereas allowing an additional soft (1 keV) component reduces this to  $\chi^2_\nu = 2.7$ . We used the 2-component model and ignore the cool component obtained in the fit since its contribution to the baryonic mass is very small. Similar results are obtained if R2 is included in these fits. A399 was excised from the image out to a radius of  $25'$  prior to the analysis.
- **A478:** A significant excess over the Galactic neutral hydrogen column density is observed. For this cluster only, we adopt the best-fit hydrogen column density instead of the Galactic value.
- **A1656:** The emission from an infalling group of galaxies to the south-west of the cluster was excised from the image prior to the analysis.
- **A2029:** A spatially variable background is seen in both PSPC exposures of this field; the field of view also includes (just to the north of A2029) Abell 2033. Extended emission around

and between these two clusters is clearly seen. Spectra extracted by beta model fits to the profile are not significantly affected by this.

- **A3558:** A soft component of emission is required in the fit . A single-phase fit to the cluster as a whole with Galactic absorption gives  $\chi^2_{\nu} = 11.1$  for 3 D.O.F. ; a two-component fit gives  $\chi^2_{\nu} = 4.7$  for 2 D.O.F. and a soft component detected at the  $5\sigma$  level. A3558 is at the center of the Shapley supercluster, with four other Abell clusters and several smaller clusters within a  $2^\circ$  radius. Significant emission over most of the field of view (particularly to the south-east) is clearly evident.
- **A3571:** Located just over  $4^\circ.3$  ( $= 8.6h^{-1}$  Mpc) away from A3558, this cluster is at a similar redshift of  $z \sim 0.04$  and appears also to be associated with the Shapley supercluster. There is some extended emission in the field.
- **A3921:** A soft component is required in the fit.

#### 4.4. Assessment of Errors

The following three subsections describe our assessment of the statistical and systematic uncertainties in the our models and the model predictions (§ 4.4.1) and the overall calibration uncertainty (§ 4.4.2).

##### 4.4.1. Monte Carlo Simulations

To study statistical uncertainties in the profile parameters, masses, and SZE predictions for each cluster, the composite 0.5–2.0 keV (R4–R7) count rate image for the longest exposure on each cluster was smoothed with a  $30''$  FWHM Gaussian. A set of  $10^3$  simulated observations were created by multiplying the smoothed count rate image by the averaged R4–R7 exposure maps calculated by EXSAS and adding Poisson noise. Each realization was then subjected to an automated analysis designed as much as possible to mimic our actual data reduction. Exposure and

point source masks were applied to the data, and the centroid computed within a circular aperture with a radius randomly varying between  $2'$  and  $30'$ . The center of this circle was taken to be the emission centroid we had determined by hand (§ 4.1); a random perturbation with a Gaussian  $\sigma$  of  $30''$  in both coordinates was applied to this center to account for the uncertainty in the visually determined luminosity peak. The azimuthal profile was computed about this centroid and fit to a model as described in § 4.1. For clusters on which we had chosen to perform fits to the exterior data, we also evaluated these fits with the same method.

This results in a distribution of  $10^3$  profile parameterizations for each cluster which we use to determine the 68% confidence intervals for  $\theta_0$  and  $\beta$ . Using this distribution plus the confidence interval for the cluster luminosity obtained from the spectral analysis, we determined confidence intervals for the central density, baryonic mass, total mass, and baryon mass fraction. In calculating the total mass confidence interval, 90% confidence intervals for  $T_e$  were translated into  $1 - \sigma$  error bars assuming Gaussian statistics, and these were added in quadrature to the error bars resulting from our Monte Carlo simulations of the cluster profiles. We also computed the distribution of 5.5-meter and ACBAR beam-averaged optical depths for each cluster by generating 2-D realizations of the profile parameterizations resulting from our Monte Carlo analysis and convolving these with the telescope beam and switching patterns. The uncertainty in the 5.5-meter main beam characterization ( $\sigma_{5.5-m} = 3'.12 \pm 0'.11$ ) was included in these calculations; for ACBAR we assumed a  $4'$  FWHM primary beam. The 5.5-meter  $\tau_{sw}$  predictions were computed with a beam throw of  $22'.12$ .

We used a similar strategy to quantify the sensitivity of our results to residual PSPC backgrounds and errors in the vignetting correction. In each case a fiducial model with  $\theta_0 = 5'.0$ ,  $\beta = 0.720$ , and a central “intensity” of 50.0 counts per pixel was created as a sky brightness template; this is characteristic of a short ( $\sim 8$  ksec) exposure of a merger cluster in our sample. For the background study, 10% of the actual background which EXSAS subtracted from the A85a data set was then added to this image, along with a constant background of 0.05 counts/pixel. For the vignetting study, a quadratic vignetting error ( $\pm 5\%$  at the edges of the field of view) was applied



to the image. In the analysis of many PSPC data sets, Vikhlinin et al. (1999) find no evidence for vignetting errors of greater than  $\sim 5\%$ , so this is not unrealistic.  $10^4$  instantiations of this map were generated including Poisson noise; these images were then azimuthally averaged and fit to beta models. In all three cases the average beta model parameters were affected by less than 0.1%. This implies not only that our *profile* parameters are insensitive to these potential sources of systematic error, but also that our (beta model-derived) *spectra* are unaffected by them at this level. The insensitivity of our derived parameters to the addition of a variable background can be understood in light of the fact that while the instrumental backgrounds are not in general constant, neither are they correlated with a beta model. The insensitivity of our results to the vignetting correction is simply due to the fact that this correction matters most in the outer wings of the azimuthal profile, which drive the constant term in the fit.

We also used these simulations to quantify the error in the total number of counts inferred by fitting a beta model to the data. We find that the fractional error in the total number of counts  $N$  is well represented by:

$$\frac{\epsilon_N}{N} = \sqrt{\frac{2}{N}} \quad (24)$$

for the given background levels.

#### 4.4.2. Calibration Uncertainties

In assessing the level at which systematic errors affect our results, there are two basic issues: repeatability and the overall (non-variable) calibration uncertainty. Some degree of non-repeatability from one observation to the next may be introduced if, for instance, the PSPC gains were to change slightly and in a systematic way across the band, which would affect our spectral fits and hence our derived luminosities. The overall calibration is dependent primarily on the mirror effective areas and energy response matrices used to generate the `.rmf` and `.arf` files used to calibrate the data.

We use the following data sets to evaluate the repeatability of our measurements: A85 A–C; A401 A,B; A754 A–D; A1795 C–E; A2142 A,C; and A2256 A,F. The standard deviation in the

ratio of the fluxes in the individual observations to the mean flux for each object is 2.9%. We take this to characterize the  $1\sigma$  precision of our measurements. There is no systematic trend discernable between PSPC B, PSPC C, or PSPC BH exposures.

Snowden et al. (1995) estimate the ROSAT PSPC absolute calibration uncertainty by comparing the RASS fluxes to the fluxes observed in other all-sky surveys. In the 1.5-keV band, the PSPC results agree with the HEAO-1 results to 1%, but with Wisconsin to only 7%; Snowden et al. attribute this to the Wisconsin calibration being off by this amount. In the  $\frac{1}{4}$  keV band, the ROSAT fluxes appear consistently to be  $\sim 10\%$  lower than the other two surveys'. We take the overall absolute calibration uncertainty to be 7%.

Adding our 2.9% precision estimate to the 2.3% error due to the ambiguity in the x-ray spectrum interpretation, there is a 3.7% (random) calibration uncertainty associated with each cluster. Adding this in quadrature with the Snowden et al. systematic calibration uncertainty of 7%, we obtain an overall calibration uncertainty of 7.9% for any given cluster. Since the electron density is proportional to the square root of the x-ray flux, this is also the error in  $H_o$  due to the x-ray calibration.

## 5. Results

In this section we summarize the results of our analysis, beginning with the profile parameterizations (§ 5.1). Next we present the SZE predictions for these clusters (§ 5.2). Lastly (§ 5.3), we give baryonic masses, total masses, and mass fractions for these 22 clusters.

### 5.1. Cluster Profiles

The beta model parameters and uncertainties which result from our analysis are summarized in Table 6. This table shows the mean of the parameter distributions for the primary models, along with, when relevant, the parameters obtained by excising the inner  $150 h^{-1}$  kpc; these are

the primary and alternate models described in § 4.1. The angular radius corresponding to this cut is shown as  $\theta_{cut}$ , and the number of components (beta, or beta plus Gaussian for the cooling flow) is also shown.

It is notable that the  $\beta$  values for the alternate models (those with the central data excised) tend to be higher than those for the primary models. To see if this is significant, we characterize the model slopes by

$$\beta_{eff}(\theta) = \beta \frac{\theta^2/\theta_0^2}{1 + \theta^2/\theta_0^2}. \quad (25)$$

or minus 1/3 the logarithmic derivative of the density profile at the radius  $\theta$  (see Eq. 29). Table 7 shows  $\beta_{eff}$  for the 10 cooling flow clusters evaluated at  $1 h^{-1}$  Mpc for the primary and alternate models, as well as the ratio of these quantities  $r$ . The weighted average yields  $r = 0.94 \pm 0.01$ , a statistically significant result implying that the total mass estimates depend at the  $\sim 5\%$  level on the profile modeling strategy we choose for the cooling flow clusters. While we will not attempt to show this here, we find that the single beta model fits to the entire profile for cooling flow clusters are significantly more biased than fits with a separate component to represent the central emission. Since the fits to the outer data presumably yield a better measure of the gas slope in this regime, we use the alternate profiles for the total mass calculation on these 10 clusters.

Model	$\theta_{cut}$ ( $^{\circ}$ )	$N_{comp}$	$\theta_0$ ( $^{\circ}$ )	$\beta$
A85	0	2	$2.04 \pm 0.52$	$0.60 \pm 0.05$
A85.2	3.62	1	$5.42 \pm 0.38$	$0.779 \pm 0.025$
A399	0	1	$4.33 \pm 0.45$	$0.742 \pm 0.042$
A401	0	1	$2.26 \pm 0.41$	$0.636 \pm 0.047$
A478	0	2	$1.00 \pm 0.15$	$0.638 \pm 0.014$
A478.2	2.22	1	$1.58 \pm 0.20$	$0.683 \pm 0.011$
A754	0	1	$5.50 \pm 1.10$	$0.713 \pm 0.120$
A780	0	2	$1.64 \pm 0.38$	$0.629 \pm 0.028$
A780.2	3.60	1	$0.90 \pm 0.33$	$0.640 \pm 0.007$
A1651	0	2	$2.16 \pm 0.36$	$0.712 \pm 0.036$
A1651.2	2.39	1	$1.86 \pm 0.34$	$0.690 \pm 0.020$
A1656	0	1	$9.32 \pm 0.10$	$0.670 \pm 0.003$
A1795	0	2	$2.17 \pm 0.28$	$0.698 \pm 0.017$
A1795.2	3.10	1	$2.98 \pm 0.20$	$0.750 \pm 0.011$
A2029	0	2	$0.93 \pm 0.09$	$0.601 \pm 0.030$
A2029.2	2.55	1	$2.09 \pm 0.36$	$0.667 \pm 0.016$
A2142	0	2	$1.60 \pm 0.12$	$0.635 \pm 0.012$
A2142.2	2.22	1	$1.91 \pm 0.60$	$0.655 \pm 0.030$
A2244	0	1	$0.82 \pm 0.14$	$0.580 \pm 0.018$
A2255	0	1	$4.36 \pm 0.12$	$0.723 \pm 0.015$
A2256	0	1	$5.49 \pm 0.21$	$0.847 \pm 0.024$
A2597	0	2	$0.49 \pm 0.03$	$0.626 \pm 0.018$
A2597.2	2.33	1	$1.61 \pm 0.52$	$0.693 \pm 0.022$
A3112	0	1	$0.52 \pm 0.05$	$0.560 \pm 0.008$
A3112.2	2.75	1	$1.24 \pm 0.49$	$0.590 \pm 0.017$
A3158	0	1	$2.84 \pm 0.16$	$0.649 \pm 0.018$
A3266	0	1	$8.50 \pm 0.27$	$0.942 \pm 0.020$
A3558	0	1	$2.66 \pm 0.07$	$0.55 \pm 0.006$
A3571	0	2	$3.64 \pm 0.18$	$0.669 \pm 0.009$
A3571.2	4.6	1	$4.35 \pm 0.50$	$0.702 \pm 0.020$
A3667	0	1	$4.29 \pm 0.96$	$0.589 \pm 0.051$
A3921	0	1	$1.33 \pm 0.23$	$0.541 \pm 0.031$

Table 6: Enumeration of the primary and (for cooling flow clusters) secondary models employed in the analysis. Errors are 68% confidence intervals.

Cluster	$\beta_{eff}(1 h^{-1} \text{Mpc})$		$r$
	All	Outer	
A85	$0.60 \pm 0.05$	$0.74 \pm 0.02$	$0.81 \pm 0.07$
A478	$0.64 \pm 0.01$	$0.67 \pm 0.01$	$0.96 \pm 0.02$
A780	$0.63 \pm 0.03$	$0.63 \pm 0.01$	$1.00 \pm 0.05$
A1651	$0.70 \pm 0.03$	$0.68 \pm 0.02$	$1.03 \pm 0.05$
A1795	$0.69 \pm 0.01$	$0.73 \pm 0.01$	$0.94 \pm 0.02$
A2029	$0.60 \pm 0.01$	$0.66 \pm 0.02$	$0.91 \pm 0.03$
A2142	$0.63 \pm 0.01$	$0.65 \pm 0.02$	$0.97 \pm 0.03$
A2597	$0.62 \pm 0.02$	$0.68 \pm 0.02$	$0.91 \pm 0.04$
A3112	$0.56 \pm 0.01$	$0.60 \pm 0.01$	$0.93 \pm 0.02$
A3571	$0.66 \pm 0.01$	$0.69 \pm 0.02$	$0.96 \pm 0.03$
AVERAGE			$0.94 \pm 0.01$

Table 7:  $\beta_{eff}$  as a function of model choice for the 10 cooling flow clusters in our sample. The “All” models are beta plus Gaussian fits to the entire profile; the “Outer” models are beta model fits to the outer data only. Errors are 68% confidence intervals.

## 5.2. Sunyaev-Zeldovich Effect Models and Predictions

The inverse Compton optical depths we compute for the 5.5-meter and ACBAR are displayed in Table 8; for clusters with a central excess we show predictions using both the primary and secondary models. The fitting problem is somewhat complicated in that there are many characteristic scales; some of them are angular, such as the beam width and chop, and some metric, such as the excision radius and any intrinsic cluster scales. The accuracy with which the beam-averaged and switched optical depths are predicted depends on this hierarchy of scales as well as the intrinsic signal-to-noise level of the data. Nevertheless some overall trends are apparent.

First, the inverse Compton optical depths are predicted to significantly better accuracy than might be naively expected on the basis of the profile analysis, the parameters of which are often uncertain at the 10% level or greater (see Table 6). In contrast to this the 5.5-meter optical depths in Table 8 are predicted with an average accuracy (for the 5.5-meter  $\tau_{sw}$ ) of 5.4%; if the main beam uncertainty is excluded from our simulations, the average uncertainty is  $\sim 2\%$ . The fact that the models can be constrained more accurately than the individual model parameters is caused by the well-known parameter degeneracies inherent in the beta model analysis. To further illustrate this point, we show in Figure 1 the distribution of  $\tau_{sw}$  for the 5.5-meter for the alternate model A2142.2 (excluding, however, the main beam uncertainty). Due to the central excision, the core radius in this case is very poorly constrained; even so,  $\tau_{sw}$  is predicted to an accuracy of 2.3%. It is notable that the uncertainties on the ACBAR optical depths are typically a factor of  $\sim 2$  smaller than those on the 5.5-meter beam-averaged optical depths. The reason for this is that we have not included in the ACBAR beam uncertainty in our simulations, since this is not yet known. The discrepancy is most notable in the cases where the clusters subtend a large angle on the sky, such as A754 and A2256; for these two cases, the uncertainty in  $\tau_{Beam}$  for the 5.5-meter is more than three times that in  $\tau_{Beam}$  for ACBAR. The 5.5-meter primary beam uncertainty is in part responsible for the larger statistical uncertainties for the A85, A754, and A780 models, as these clusters all lie at  $z < 0.06$ . The beam uncertainty dominates the statistical error in  $\tau_{Beam}$  and  $\tau_{sw}$  for the Coma cluster (A1656), which to a good approximation fills the main beam of the 5.5-meter telescope.

Second, the uncertainties in  $\tau_{sw}$  are often *less* than those in the associated  $\tau_{Beam}$ . This occurs because the noise in  $\beta$  is suppressed somewhat in the switched SZE predictions. For a fixed x-ray flux, increasing  $\beta$  reduces the predicted central decrement by reducing the baryonic mass surface density. At the same time, this increase reduces the flux in the chopping beam, thereby increasing the switched decrement and cancelling some of the reduction due to the lesser central decrement. A similar effect will be present for interferometers, which effectively measure sky temperature differences on the angular scale of the fringe pattern.

Partly due to this effect, and partly due to the fact that the 5.5-meter beam is larger than the excision radius for most of these clusters, our  $\tau_{sw}$  results for the 5.5-meter are statistically unaffected by our chosen modeling strategy. All of the  $\tau_{sw}$  predictions for the alternate models in Table 8 are consistent (or, for A780, marginally consistent) with the primary model predictions. This is certainly not the case for  $\tau_o$ , for which the two strategies typically yield  $\tau_o$  estimates which differ by  $\sim 30\%$  or more. For clusters at  $z < 0.051$ , the excised region of the profile is equal to or larger than the diameter of the 5.5-meter primary beam. This explains the relatively large discrepancy between A780 and A780.2 (a  $z = 0.0522$  cluster). Note that even in these cases, the alternate model will, under the assumption of spherical symmetry, correctly measure the contributions from the extended lines of sight in the beam.

The ACBAR beam-averaged optical depths are somewhat less robust in this respect. This is not surprising because the  $150 h^{-1}$  kpc excision radius is larger than the ACBAR primary beam for all of the clusters in this sample. Better results could certainly be obtained with a more moderate excision. Even though we have not explicitly demonstrated that these results are robust as we have for the 5.5-meter predictions, the primary models we present here should be more than adequate for experiments like ACBAR with  $\sim 4'$  angular resolution given the beam uncertainties and measurement errors likely to exist in practice.

Abell 754 is the cluster with the least accurate profile. This is a well studied major merger cluster (e.g., Fabricant et al. 1986; Henry & Briel 1995; Henriksen & Markevitch 1996) with clear large-scale substructure in both x-ray and optical images. We include it in the current analysis for

completeness, although any total mass estimates for this cluster should be interpreted with caution. Even for this cluster, the 10% uncertainty in  $\tau_{sw}$  is only just comparable to typical SZ measurement errors.

Cluster Model	5.5-meter			ACBAR
	$\tau_o$ ( $10^{-3} h^{-1/2}$ )	$\tau_{beam}$ ( $10^{-3} h^{-1/2}$ )	$\tau_{sw}$ ( $10^{-3} h^{-1/2}$ )	$\tau_{beam}$ ( $10^{-3} h^{-1/2}$ )
A85	6.60 ± 0.48	3.81 ± 0.22	2.88 ± 0.23	4.94 ± 0.12
A85.2	4.72 ± 0.14	3.45 ± 0.09	2.76 ± 0.13	4.14 ± 0.10
A399	4.34 ± 0.28	3.08 ± 0.17	2.50 ± 0.13	3.77 ± 0.05
A401	6.96 ± 0.55	4.15 ± 0.24	3.17 ± 0.18	5.34 ± 0.13
A478	12.93 ± 1.17	4.39 ± 0.20	3.68 ± 0.15	6.59 ± 0.12
A478.2	10.02 ± 1.03	4.22 ± 0.22	3.61 ± 0.17	6.15 ± 0.23
A754	5.20 ± 0.37	4.16 ± 0.27	3.02 ± 0.31	4.77 ± 0.09
A780	5.49 <sup>+1.18</sup> <sub>-0.54</sub>	2.62 ± 0.13	2.11 ± 0.11	3.61 ± 0.05
A780.2	10.67 <sup>+2.42</sup> <sub>-2.97</sub>	2.98 ± 0.18	2.52 ± 0.20	4.57 ± 0.45
A1651	5.75 <sup>+0.80</sup> <sub>-0.51</sub>	2.84 ± 0.15	2.44 ± 0.11	3.98 <sup>+0.20</sup> <sub>-0.09</sub>
A1651.2	6.06 ± 0.84	2.88 ± 0.12	2.47 ± 0.11	4.07 ± 0.23
A1656	5.22 ± 0.36	4.77 ± 0.30	2.76 ± 0.16	5.07 ± 0.02
A1795	6.88 ± 0.54	3.49 ± 0.17	2.95 ± 0.13	4.84 <sup>+0.08</sup> <sub>-0.12</sub>
A1795.2	5.94 ± 0.29	3.37 ± 0.11	2.88 ± 0.10	4.52 ± 0.13
A2029	12.13 ± 1.31	4.37 ± 0.20	3.52 ± 0.14	6.34 ± 0.10
A2029.2	8.09 ± 1.51	4.09 ± 0.19	3.37 ± 0.17	5.60 ± 0.43
A2142	11.11 ± 0.09	5.28 ± 0.26	4.28 ± 0.18	7.33 ± 0.06
A2142.2	10.68 ± 2.13	5.19 ± 0.30	4.25 ± 0.22	7.16 ± 0.50
A2244	8.16 ± 0.64	2.93 ± 0.15	2.30 ± 0.11	4.20 ± 0.07
A2255	3.89 ± 0.27	2.81 ± 0.15	2.23 ± 0.11	3.40 ± 0.03
A2256	5.13 ± 0.36	3.77 ± 0.20	3.19 ± 0.16	4.54 ± 0.03
A2597	9.86 ± 0.75	2.05 ± 0.10	1.74 ± 0.09	3.26 ± 0.09
A3112	9.04 ± 0.65	2.62 ± 0.13	2.06 ± 0.10	3.82 ± 0.06
A3112.2	6.32 <sup>+2.11</sup> <sub>-1.34</sub>	2.58 ± 0.13	2.05 ± 0.14	3.63 ± 0.30
A3158	4.88 ± 0.34	3.11 ± 0.16	2.43 ± 0.12	3.95 ± 0.43
A3266	4.30 ± 0.30	3.56 ± 0.20	2.89 ± 0.16	4.03 ± 0.03
A3558	5.07 ± 0.36	3.59 ± 0.20	2.39 ± 0.13	4.31 ± 0.08
A3571	6.46 ± 0.47	4.52 ± 0.25	3.49 ± 0.17	5.54 ± 0.10
A3571.2	6.01 ± 0.29	4.39 ± 0.16	3.41 ± 0.14	5.27 ± 0.02
A3667	5.60 ± 0.46	4.52 ± 0.28	2.95 ± 0.17	5.18 ± 0.17
A3921	5.75 ± 0.41	3.06 ± 0.16	2.18 ± 0.12	3.98 ± 0.04

Table 8: Central and beam-averaged optical depths for 22 clusters. The 5.5-meter beam-averaged optical depths include the uncertainties due to the main beam determination. All quoted  $\tau$  values are the means of the observed distributions, *not* the values corresponding to our best-fit models. The models are defined in Table 6. All errors are  $1 - \sigma$ .

Our best fit profile models are summarized in Table 9. Due to the beta model parameter degeneracies, it is important to use the parameters listed in Table 9 and not, for instance, the



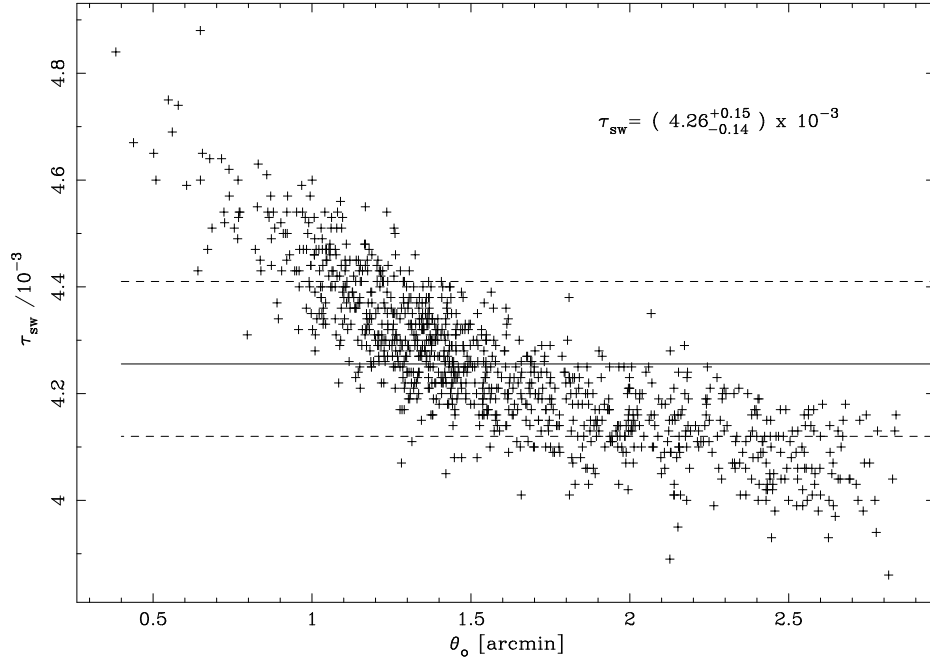


Fig. 1.— Switched 5.5-m SZE as a function of core radius for fits to A2142 excluding the inner  $150 h^{-1}$  kpc showing that so long as parameter degeneracies are correctly accounted for and a reasonable fit obtained, our results are insensitive to the form the profile at the  $\sim 3\%$  level. The mean and 68% confidence increments are shown as solid and dashed lines, respectively; the standard deviation in this distribution (which excludes the uncertainty in  $\Omega_{Beam}$  for the 5.5-m) is 2.3% of the mean.

distribution mean for  $n_{eo}$  from Table 10 together with the  $\beta$  and  $\theta_0$  from Table 6. The values for  $\tau_0$  shown in Table 9 are model normalizations and are *not* necessarily representative of the actual central inverse Compton optical depth which would be observed in very high resolution SZ maps.

The dependence of these results on the chosen cosmology will be discussed in § 6.

Cluster	$\theta_0$ (')	$R_0$ ( $h^{-1}$ kpc)	$\beta$	$n_{eo}$ ( $10^{-3} h^{1/2} \text{cm}^{-3}$ )	$\tau_o$ ( $10^{-3} h^{-1/2}$ )
A85	2.04	84.4	0.600	10.44	6.59
A399	4.33	239	0.742	3.23	4.34
A401	2.26	130.	0.636	7.90	7.05
A478	1.00	67.5	0.638	27.81	12.84
A754	5.50	232	0.713	3.81	5.20
A780	1.64	68.3	0.629	11.30	5.38
A1651	2.16	135	0.712	7.14	5.70
A1656	9.32	181	0.670	4.52	5.23
A1795	2.17	105	0.698	10.70	6.81
A2029	0.930	54.7	0.601	29.35	11.99
A2142	1.60	108	0.635	14.95	11.10
A2244	0.820	59.5	0.580	17.30	8.13
A2255	4.36	266	0.723	2.53	3.89
A2256	5.49	260	0.847	4.08	5.13
A2597	0.49	31.7	0.626	44.64	9.90
A3112	0.52	28.3	0.56	38.12	9.02
A3158	2.84	132	0.649	5.52	4.88
A3266	8.50	398	0.942	2.49	4.30
A3558	2.66	103	0.55	5.71	5.07
A3571	3.64	118	0.669	8.57	6.46
A3667	4.29	188	0.589	3.92	5.68
A3921	1.33	94.9	0.541	6.18	5.20

Table 9: Summary of best-fit models and the central densities and optical depths for these models.

### 5.3. Baryonic and Total Masses and Baryon Mass Fractions

The baryonic masses, total masses, and baryon fractions for the 22 clusters with public data in our sample are shown in Table 10 and Table 11. The baryonic mass within a spherical radius  $R$  for a beta model can be shown to be:

$$M_{bary}(< R) = \frac{4}{3}\pi R^3 \rho_B {}_2F_1\left(\frac{3}{2}, \frac{3\beta}{2}, \frac{5}{2}, -\left(\frac{R}{r_o}\right)^2\right) \quad (26)$$

where  $\rho_B$  is the baryonic mass density

$$\rho_B = n_e m_p \times \mu_e. \quad (27)$$

Here  $m_p$  is the proton mass and  $\mu_e$  is the baryonic mass in the plasma per electron, and  ${}_2F_1$  is a confluent hypergeometric function. The total masses were computed under the assumption of hydrostatic equilibrium. For the total mass contained within a sphere of radius  $r$  we find

$$M(< r) = -\frac{kT(r)}{G\mu m_p} \times r \times \left(\frac{\partial \ln n_e}{\partial \ln r} + \frac{\partial \ln T}{\partial \ln r}\right), \quad (28)$$

where  $\mu$  is the mean molecular mass ( $= 0.592$  for our assumed 30% metallicity and the Solar abundances of Anders & Grevesse (1989)). For the isothermal beta model this assumes the form

$$M(< r) = \frac{kT}{G\mu m_p} \times 3\beta \frac{\theta^2/\theta_0^2}{1 + \theta^2/\theta_0^2}. \quad (29)$$

We compute these quantities both at a fixed metric radius of  $500 h^{-1}$  kpc and at the radius  $R_{500}$  within which the mean density is 500 times the critical density. For the latter, we use the Mohr et al. (1999) definition

$$R_{500} = 1.185 h^{-1} \text{ Mpc} \times \left(\frac{T_e}{10 \text{ keV}}\right)^{\frac{1}{2}}. \quad (30)$$

This allows us to compare virially similar regions of each cluster, as well facilitating a direct comparison between our results and those of Mohr et al. (although the electron temperatures they adopt tend to be lower than ours).

Within  $500 h^{-1}$  kpc, the baryonic masses are accurate to 4% or better, with an average uncertainty of about 2%. The mean baryonic mass within this radius is  $(1.42 \pm 0.18) \times 10^{13} h^{-5/2} M_\odot$

( $1\sigma$  S.D.). The total masses are accurate to 5 – 10%, with an average uncertainty of 8%; the mean total mass inside  $500 h^{-1}$  kpc is  $(2.19 \pm 0.36) \times 10^{14} h^{-1} M_{\odot}$ . At  $R_{500}$ , the average baryonic mass is  $(2.94 \pm 0.85) \times 10^{13} h^{-5/2} M_{\odot}$ , and the average total mass is  $(4.72 \pm 1.86) \times 10^{14} h^{-1} M_{\odot}$ . The mean baryon fraction within  $500 h^{-1}$  kpc is  $(6.09 \pm 0.17) h^{-3/2} \%$  (s.d. =  $0.78 h^{-3/2} \%$ ); within  $R_{500}$ , it is  $(7.02 \pm 0.28) h^{-3/2} \%$  (s.d. =  $1.32 h^{-3/2} \%$ ).

As noted in § 4.1, the total masses we infer depend at the 5% level on the profile modeling strategy we choose, particularly for the cooling flow clusters. For these clusters we compute the total mass from fits to the data excluding the inner region of the cluster. The baryonic masses (like the SZE predictions in in § 5.2) are always computed from single- or double-component fits to all of the profile.

The total mass computation relies on the assumptions of hydrostatic equilibrium and isothermality. Evrard et al. (1996) find that isothermal beta model estimates of the total mass in numerically simulated clusters on scales of  $R_{500} - R_{2000}$  are unbiased and accurate to  $\sim 15\%$  on average, suggesting that the strategy we adopt is not likely to be seriously in error. Markevitch et al. (1998) have found evidence for departures from isothermality in their analysis of 30 nearby clusters. In a similar analysis, however, Irwin et al. (1999) do not find a similar effect. If the temperature were to fall at large radius, the total masses would be lower than the estimates we present here. Future data from XMM and Chandra will help clarify this situation.

We will discuss the effects of the chosen cosmological model on these results in the next section.

Cluster	$M_{Bary}$ ( $10^{13} h^{-5/2} M_{\odot}$ )	$M_{tot}$ ( $10^{14} h^{-1} M_{\odot}$ )	$f$ ( $h^{-3/2} \%$ )	$n_{eo}$ ( $10^{-3} h^{1/2} \text{cm}^{-3}$ )
A85 (500 $h^{-1}$ kpc)	$1.27 \pm 0.07$	$2.26^{+0.18}_{-0.23}$	$5.61 \pm 0.21$	$11.14^{+2.54}_{-1.98}$
( $R_{500} = 0.99h^{-1}$ Mpc)	$3.20 \pm 0.07$	$5.66 \pm 0.27$	$5.67 \pm 0.24$	—
A399 (500 $h^{-1}$ kpc)	$1.33 \pm 0.02$	$2.34 \pm 0.10$	$5.71 \pm 0.20$	$3.24^{+0.14}_{-0.19}$
( $R_{500} = 0.99h^{-1}$ Mpc)	$3.51 \pm 0.08$	$5.36 \pm 0.32$	$6.55 \pm 0.32$	—
A401 (500 $h^{-1}$ kpc)	$1.67 \pm 0.05$	$2.64^{+0.18}_{-0.11}$	$6.35 \pm 0.23$	$8.01^{+0.56}_{-1.02}$
( $R_{500} = 1.06h^{-1}$ Mpc)	$4.64 \pm 0.14$	$5.86^{+0.50}_{-0.32}$	$7.94^{+0.44}_{-0.62}$	—
A478 (500 $h^{-1}$ kpc)	$2.01 \pm 0.03$	$2.92^{+0.18}_{-0.33}$	$6.91^{+0.69}_{-0.40}$	$28.9^{+15.2}_{-3.9}$
( $R_{500} = 1.08h^{-1}$ Mpc)	$5.17 \pm 0.25$	$6.81^{+0.49}_{-0.78}$	$7.60^{+0.76}_{-0.45}$	—
A754 (500 $h^{-1}$ kpc)	$1.56^{+0.10}_{-0.17}$	$3.09^{+0.36}_{-0.48}$	$5.07 \pm 0.26$	$3.73^{+0.07}_{-0.1}$
( $R_{500} = 1.15h^{-1}$ Mpc)	$5.15 \pm 0.24$	$8.30^{+1.41}_{-1.32}$	$6.21^{+1.81}_{-1.23}$	—
A780 (500 $h^{-1}$ kpc)	$0.870^{+0.014}_{-0.053}$	$1.47^{+0.09}_{-0.19}$	$5.91 \pm 0.36$	$12.90^{+18.0}_{-2.97}$
( $R_{500} = 0.77h^{-1}$ Mpc)	$1.50 \pm 0.05$	$2.35 \pm 0.15$	$6.41 \pm 0.36$	—
A1651 (500 $h^{-1}$ kpc)	$1.31 \pm 0.02$	$2.09^{+0.10}_{-0.19}$	$6.27 \pm 0.28$	$7.47^{+5.17}_{-0.96}$
( $R_{500} = 0.92h^{-1}$ Mpc)	$2.79 \pm 0.07$	$4.29 \pm 0.22$	$6.53 \pm 0.30$	—
A1656 (500 $h^{-1}$ kpc)	$1.44 \pm 0.01$	$2.99 \pm 0.14$	$4.82 \pm 0.21$	$4.51 \pm 0.04$
( $R_{500} = 1.13h^{-1}$ Mpc)	$4.48 \pm 0.12$	$7.41 \pm 0.41$	$6.03 \pm 0.28$	—
A1795 (500 $h^{-1}$ kpc)	$1.34 \pm 0.01$	$2.89 \pm 0.24$	$4.66 \pm 0.35$	$11.29^{+0.61}_{-1.77}$
( $R_{500} = 1.04h^{-1}$ Mpc)	$3.16 \pm 0.14$	$6.63 \pm 0.61$	$4.77 \pm 0.36$	—
A2029 (500 $h^{-1}$ kpc)	$1.77 \pm 0.02$	$3.00 \pm 0.22$	$5.90 \pm 0.38$	$31.11^{+7.94}_{-6.40}$
( $R_{500} = 1.13h^{-1}$ Mpc)	$5.01 \pm 0.21$	$7.48 \pm 0.62$	$6.70 \pm 0.46$	—
A2142 (500 $h^{-1}$ kpc)	$2.38 \pm 0.02$	$3.25^{+0.32}_{-0.24}$	$7.30^{+0.49}_{-0.67}$	$15.03^{+0.92}_{-1.07}$
( $R_{500} = 1.16h^{-1}$ Mpc)	$7.19 \pm 0.37$	$8.08^{+0.95}_{-0.73}$	$8.90^{+0.64}_{-0.91}$	—

Table 10: Central densities, total masses, and baryon fractions for 11 clusters at  $500h^{-1}$  kpc and  $R_{500}$ . Quoted densities are the mean for the distribution, *not* the value corresponding to our quoted best-fit model. Errors are  $1 - \sigma$ .

Cluster	$M_{Bary}$ ( $10^{13} h^{-5/2} M_{\odot}$ )	$M_{tot}$ ( $10^{14} h^{-1} M_{\odot}$ )	$f$ ( $h^{-3/2}$ %)	$n_{eo}$ ( $10^{-3} h^{1/2} \text{cm}^{-3}$ )
A2244 (500 $h^{-1}$ kpc) ( $R_{500} = 0.99h^{-1}$ Mpc)	$1.31 \pm 0.03$ $3.33 \pm 0.37$	$2.25^{+1.07}_{-0.52}$ $4.51^{+2.19}_{-1.12}$	$5.84^{+1.32}_{-2.75}$ $7.39^{+1.70}_{-3.49}$	$17.73^{+1.95}_{-2.65}$ —
A2255 (500 $h^{-1}$ kpc) ( $R_{500} = 1.01h^{-1}$ Mpc)	$1.23 \pm 0.01$ $3.54 \pm 0.26$	$2.27^{+0.62}_{-0.30}$ $5.51^{+1.51}_{-0.73}$	$5.41^{+0.86}_{-1.65}$ $6.43^{+0.85}_{-1.76}$	$2.52 \pm 0.03$ —
A2256 (500 $h^{-1}$ kpc) ( $R_{500} = 0.96h^{-1}$ Mpc)	$1.62 \pm 0.01$ $3.79 \pm 0.08$	$2.44 \pm 0.10$ $5.53 \pm 0.27$	$6.61 \pm 0.24$ $6.83 \pm 0.30$	$4.08^{+0.09}_{-0.06}$ —
A2597 (500 $h^{-1}$ kpc) ( $R_{500} = 0.78h^{-1}$ Mpc)	$0.902 \pm 0.025$ $1.53 \pm 0.07$	$1.52^{+0.10}_{-0.16}$ $2.60^{+0.19}_{-0.29}$	$5.96^{+0.56}_{-0.34}$ $5.91^{+0.57}_{-0.36}$	$45.13^{+2.81}_{-4.75}$ —
A3112 (500 $h^{-1}$ kpc) ( $R_{500} = 0.86h^{-1}$ Mpc)	$0.974 \pm 0.017$ $2.03 \pm 0.13$	$1.64^{+0.14}_{-0.20}$ $2.96^{+0.29}_{-0.39}$	$5.95^{+0.66}_{-0.46}$ $6.84^{+0.78}_{-0.56}$	$38.38^{+2.30}_{-2.90}$ —
A3158 (500 $h^{-1}$ kpc) ( $R_{500} = 0.88h^{-1}$ Mpc)	$1.16 \pm 0.02$ $2.50 \pm 0.06$	$1.65^{+0.07}_{-0.09}$ $3.38^{+0.17}_{-0.19}$	$7.06^{+0.26}_{-0.21}$ $7.38^{+0.35}_{-0.31}$	$5.54 \pm 0.24$ —
A3266 (500 $h^{-1}$ kpc) ( $R_{500} = 1.06h^{-1}$ Mpc)	$1.54 \pm 0.01$ $4.69 \pm 0.10$	$2.55 \pm 0.10$ $7.72 \pm 0.37$	$6.06 \pm 0.22$ $6.08 \pm 0.23$	$2.49 \pm 0.05$ —
A3558 (500 $h^{-1}$ kpc) ( $R_{500} = 0.88h^{-1}$ Mpc)	$1.12 \pm 0.02$ $2.63 \pm 0.10$	$1.60 \pm 0.08$ $2.89 \pm 0.15$	$7.00 \pm 0.32$ $9.12 \pm 0.42$	$5.71 \pm 0.14$ —
A3571 (500 $h^{-1}$ kpc) ( $R_{500} = 0.98h^{-1}$ Mpc)	$1.42 \pm 0.01$ $3.33 \pm 0.04$	$2.42 \pm 0.05$ $5.15 \pm 0.16$	$5.86 \pm 0.10$ $6.48 \pm 0.17$	$8.59^{+0.17}_{-0.24}$ —
A3667 (500 $h^{-1}$ kpc) ( $R_{500} = 0.99h^{-1}$ Mpc)	$1.54 \pm 0.05$ $4.61 \pm 0.21$	$2.00 \pm 0.13$ $4.35 \pm 0.45$	$7.73 \pm 0.39$ $10.58 \pm 0.79$	$4.00 \pm 0.57$ —
A3921 (500 $h^{-1}$ kpc) ( $R_{500} = 0.94h^{-1}$ Mpc)	$1.11 \pm 0.05$ $2.90 \pm 0.34$	$1.82 \pm 0.30$ $3.50 \pm 0.65$	$6.11 \pm 0.92$ $8.30 \pm 1.32$	$6.25^{+0.92}_{-0.70}$ —

Table 11: Central densities, total masses, and baryon fractions for 11 clusters at  $500h^{-1}$  kpc and  $R_{500}$ . Errors are  $1 - \sigma$ .

## 6. Discussion and Conclusions

We have defined an x-ray flux-limited sample of 31 nearby galaxy clusters and analyzed ROSAT PSPC data on 22 of these. The primary focus of our analysis is the quantification of SZE modeling uncertainties. Using a suite of Monte Carlo simulations, we find that on average we predict the inverse Compton optical depth with an accuracy of 5.4% for the OVRO 5.5-meter telescope. These predictions are robust with respect to our cooling-flow modeling strategy and unaffected by realistic PSPC systematics. We have also presented similarly accurate predictions of the inverse Compton optical depth for the near-future ACBAR experiment. While somewhat less robust than the 5.5-meter predictions due to the small angular scales this telescope samples, these predictions should be more than sufficient for real-world applications.

We have also confirmed the Allen et al. (1993) report of an excess column density of  $N_H$  towards A478, but do not find evidence for similar anomalies in any of 21 other clusters. There appears to be an excess of soft counts in the ROSAT PSPC spectra, similar that reported by Iwasawa et al. (1999).

The mean baryon fraction within  $500 h^{-1}$  kpc is found to be  $(6.09 \pm 0.17) h^{-3/2} \%$  (s.d. =  $0.78 h^{-3/2} \%$ ); within  $R_{500}$ , it is  $(7.02 \pm 0.28) h^{-3/2} \%$  (s.d. =  $1.32 h^{-3/2} \%$ ). For  $h = 0.5$ , these are  $(17.3 \pm 0.47)\%$  and  $(19.8 \pm 0.8)\%$  respectively. These are consistent with the 10% – 20% baryon fractions observed (inside  $1 h^{-1}$  Mpc with  $h = 0.5$ ) by White & Fabian (1995) in analyses of Einstein IPC data on galaxy clusters. Our results are also in good agreement with those of Mohr et al. (1999), who find baryon fractions of  $\sim 21\%$  within  $R_{500}$  for an analysis of the 44 clusters in the Edge sample with ROSAT PSPC data. Our mass fractions tend to be slightly lower on average. In part this is due to the fact that the x-ray temperatures used by others in the literature are often biased low by cooling flow emission; the remainder is due to the difference in cluster modeling strategies. For  $h \sim 0.7$  our findings also agree with gas mass fractions determined by Grego (1998) on the basis of interferometric observations of the SZE in distant clusters. In a sample of 14 clusters, they find a gas mass fraction of  $7.1_{-1.1}^{+1.0} h^{-1} \%$  within  $R_{500}$  (at 68% confidence).



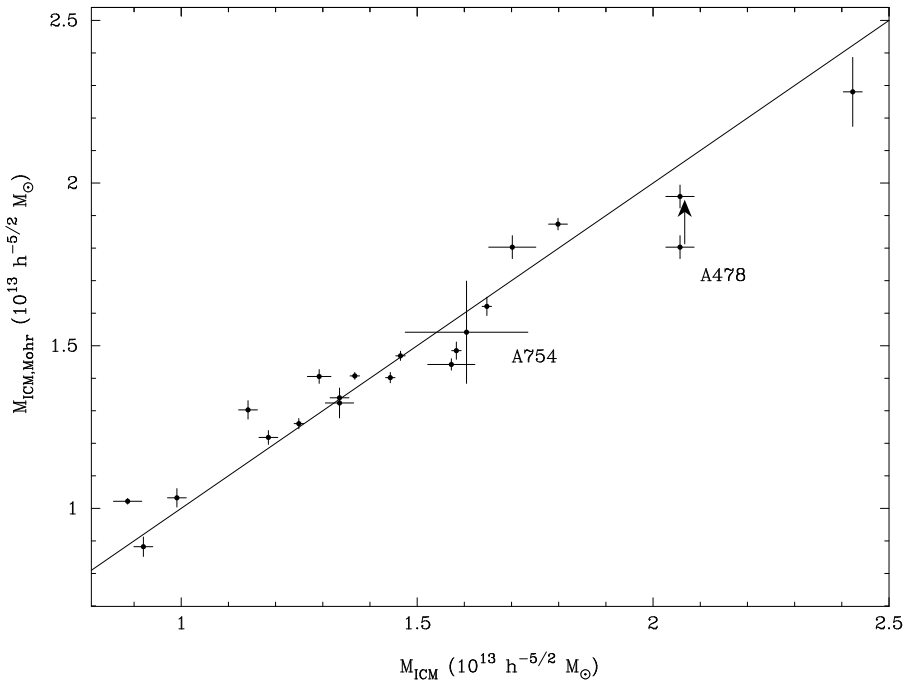


Fig. 2.— A comparison of the ICM masses obtained by Mohr et al. (1999) and in this analysis for 20 of our 22 clusters. Masses are evaluated at  $500 h^{-1}$  kpc. The arrow shows the effect of correcting the Mohr et al. A478 mass for the observed excess neutral hydrogen absorption. A754, the most clearly dynamically disturbed cluster in our sample, is also labelled.

While a number of other systematic x-ray cluster analyses exist in the literature (e.g., White et al. 1997; Mohr et al. 1999), ours is the first to attempt to realistically quantify the effect of the uncertainties in the x-ray modeling on the predicted SZE decrement for a given instrument. Since the analysis of Mohr et al. is closest to ours in spirit and technique, we have conducted a detailed comparison of their results to ours. Figure 2 shows the Mohr et al. determination of the baryonic mass internal to  $500 h^{-1}$  kpc versus our determination of this quantity. The overall agreement is excellent: the mean mass ratio ( $M_{ICM,Mohr et al.}/M_{ICM,this work}$ ) is  $1.007 \pm 0.016$  (S.D. = 7%), strongly arguing against any systematic differences in our analyses. One of the most significant outliers is A478, for which Mohr et al. have used the anomalously low Galactic value for  $N_H$ ; the effect of correcting for this is shown by an arrow in Figure 2. The scatter between our results, however, is somewhat larger than the  $\sim 4\%$  scatter which is expected. This may be in part due to different strategies for profile modeling, spectral extraction, and dealing with cooling flows.

We have attempted to directly assess the robustness of our results, but there are several considerations beyond the scope of this analysis which could affect our conclusions. The most significant is the possibility of substructure in the ICM. Mathiesen et al. (1999) have studied this in simulations of ROSAT PSPC cluster observations and find a mean overestimate of the cluster density of  $\sim 10\%$ . Since these simulations do not include astrophysically important mechanisms such as cooling and conduction, it will be important to address this issue with the current and upcoming x-ray missions Chandra and XMM, as well as more powerful simulations. Also of some concern is the possibility of large-scale temperature gradients in the cluster. While this will not significantly affect the baryonic mass models we present here, it will affect thermal SZE predictions and the inferred total masses.

For consistency with Myers et al. and many other authors we have assumed  $q_o = 0.5$ . There is increasing evidence, however, that this may be wrong (for a summary of the evidence see Bahcall et al. 1999). Due to the  $h^{-5/2}$  dependence of the baryonic mass on the distance scale, these results will be most affected by any errors in the cosmology we assume; the inverse Compton optical depths and central densities will be least affected. We have recomputed the sample average of the

baryonic mass, baryonic mass fraction, and inverse Compton optical depth for two currently viable cosmologies: an open ( $\Omega_m = 0.3$ ) model and a closed  $\Lambda$  ( $\Omega_m = 0.3, \Omega_\Lambda = 0.7$ ) model. For the closed  $\Lambda$  model, the sample average baryonic mass is increased by 8.8%, the baryonic mass fraction by 5.1%, and the inverse Compton optical depth by 1.7%. For the open model, the baryonic mass is increased by 3.0%, the baryonic mass fraction by 1.8%, and the inverse Compton optical depth by only 0.6%. Clearly this translation must be done on a cluster-by-cluster basis for a comparison of our  $\tau$  predictions with SZ data.

In paper II we will use the models presented in this work, together with improved ASCA temperatures, to obtain a measurement of  $H_o$  from SZE measurements conducted with the OVRO 5.5-meter telescope. The wider implications for cosmology of this work will also be discussed therein.

We acknowledge helpful discussions with Maxim Markevitch, Joe Mohr, Steve Snowden, and Alexey Vikhlinin; we also thank Alexey Vikhlinin for the use of his software. We thank Patricia Udomprasert for help in some of the data reduction. BSM was supported for part of the duration of this work by the Zacheus Daniels fund at the University of Pennsylvania; STM was supported by an Alfred R. Sloan fellowship at the University of Pennsylvania.

### A. Cluster Radial Profiles

In this appendix we present the profiles resulting from our analysis (Figures 3, 4, 5, and 6). The details of this analysis are described in § 4. Although it is conventional in the literature to present such fits on a log-log scale, we have chosen to employ a log-linear scale since this makes the goodness-of-fit at large radius more readily apparent.

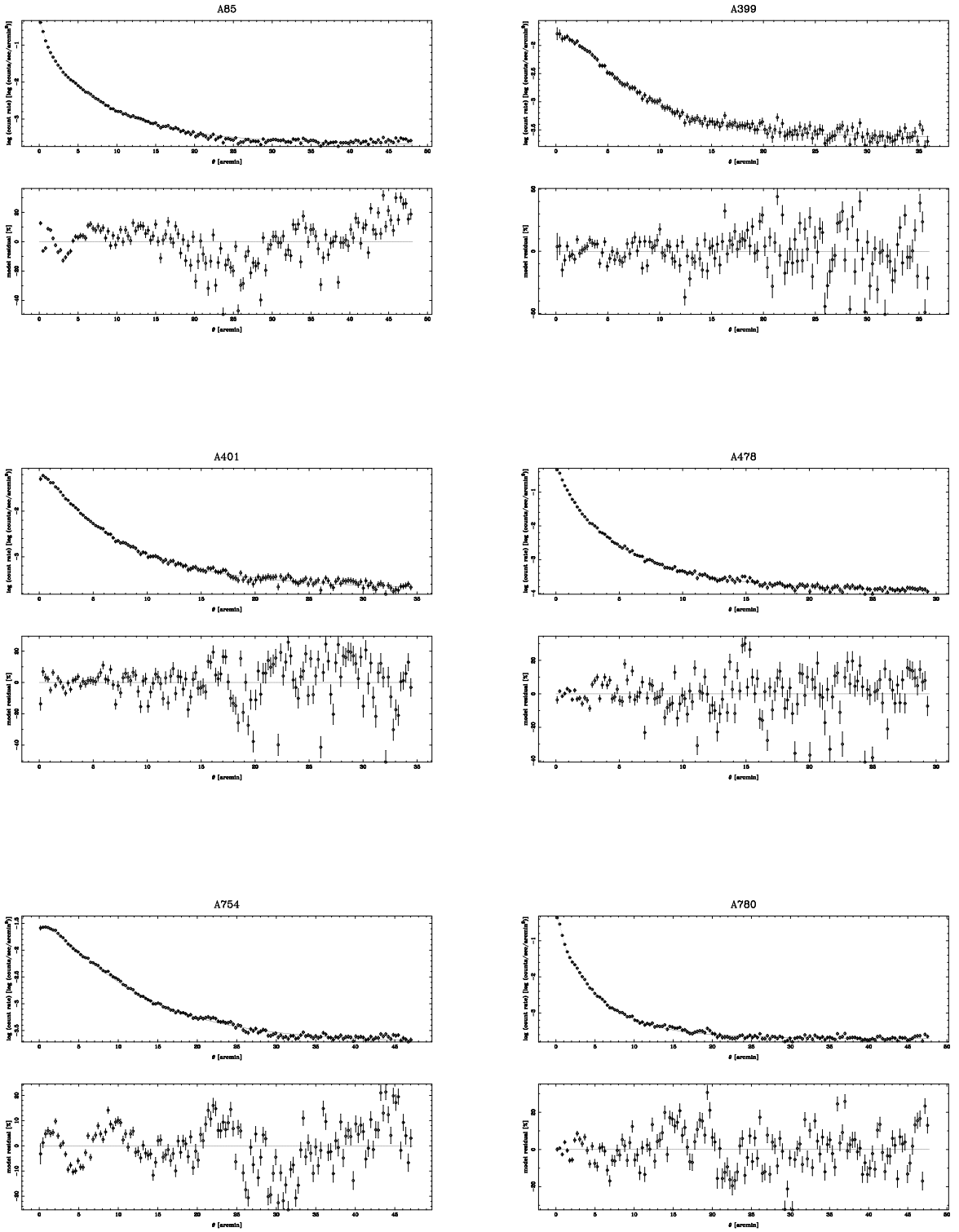


Fig. 3.— Radial profiles for A85, A399, A401, A478, A754, and A780. The x-axis is in units of arcminutes and the y-axis the log of the azimuthally averaged count rate in units of counts/sec/arcmin<sup>2</sup>.

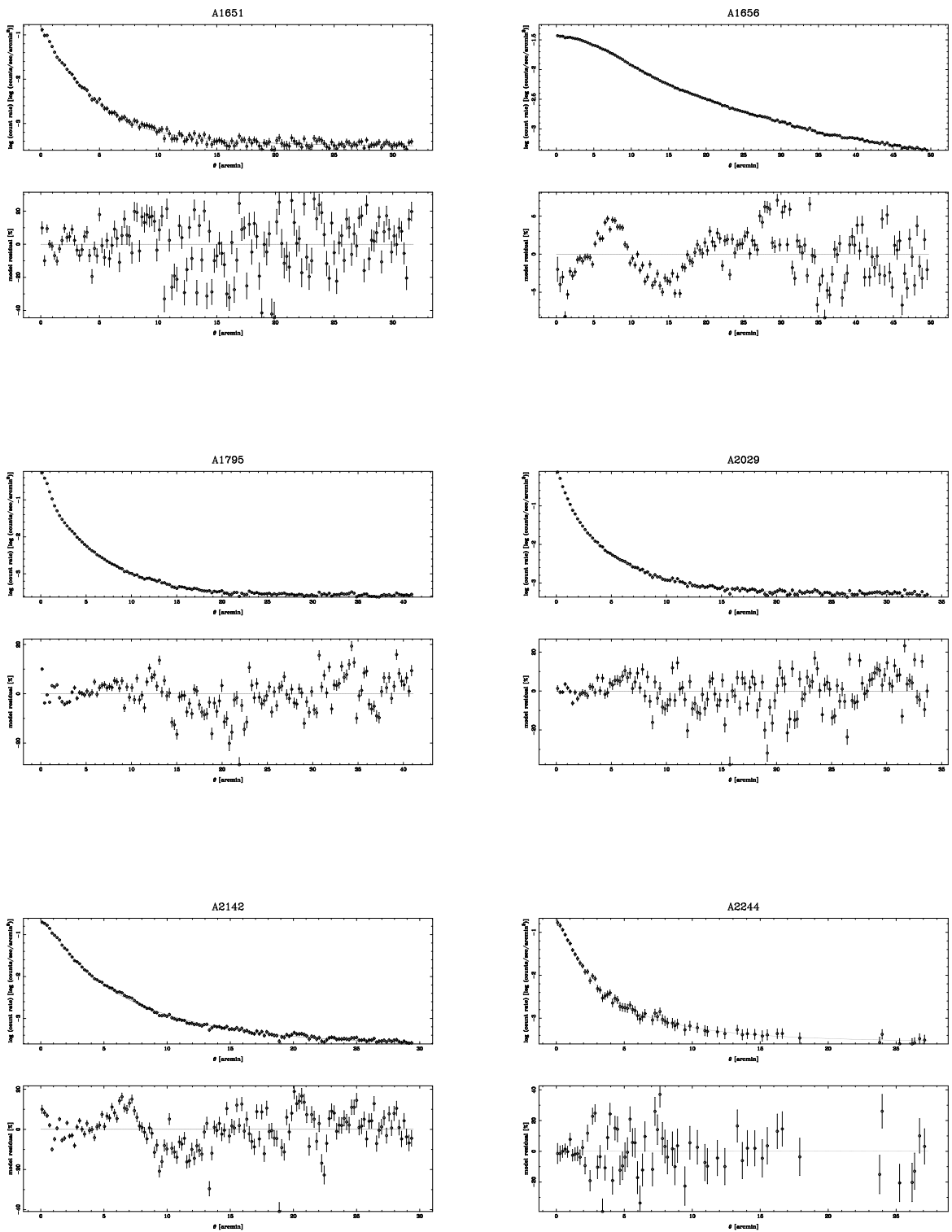


Fig. 4.— Radial profiles for A1651, A1656, A1795, A2029, A2142, and A2244. The x-axis is in units of arcminutes and the y-axis the log of the azimuthally averaged count rate in units of counts/sec/arcmin<sup>2</sup>.

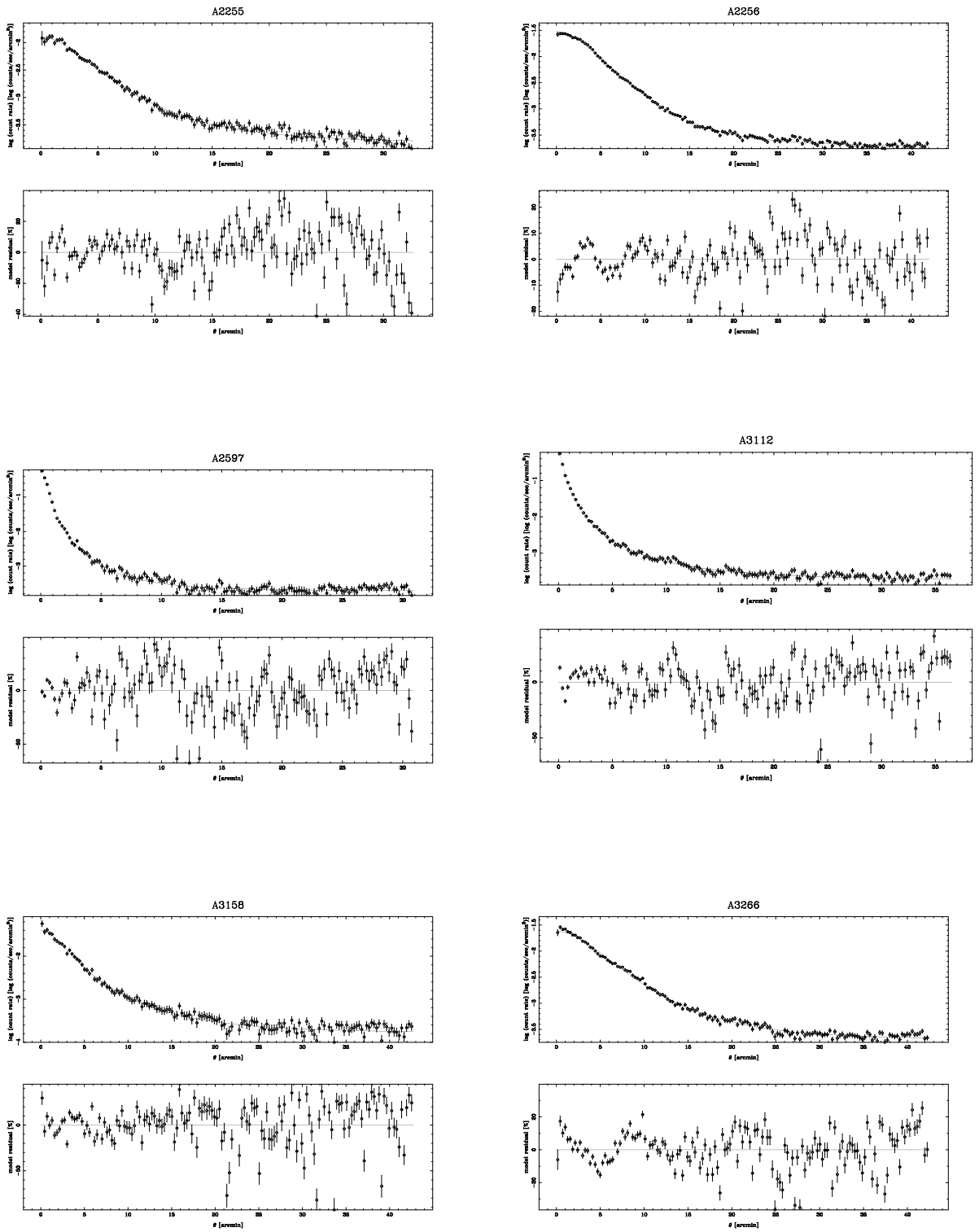


Fig. 5.— Radial profiles for A2255, A2256, A2597, A3112, A3158, A3266. The x-axis is in units of arcminutes and the y-axis the log of the azimuthally averaged count rate in units of counts/sec/arcmin<sup>2</sup>.

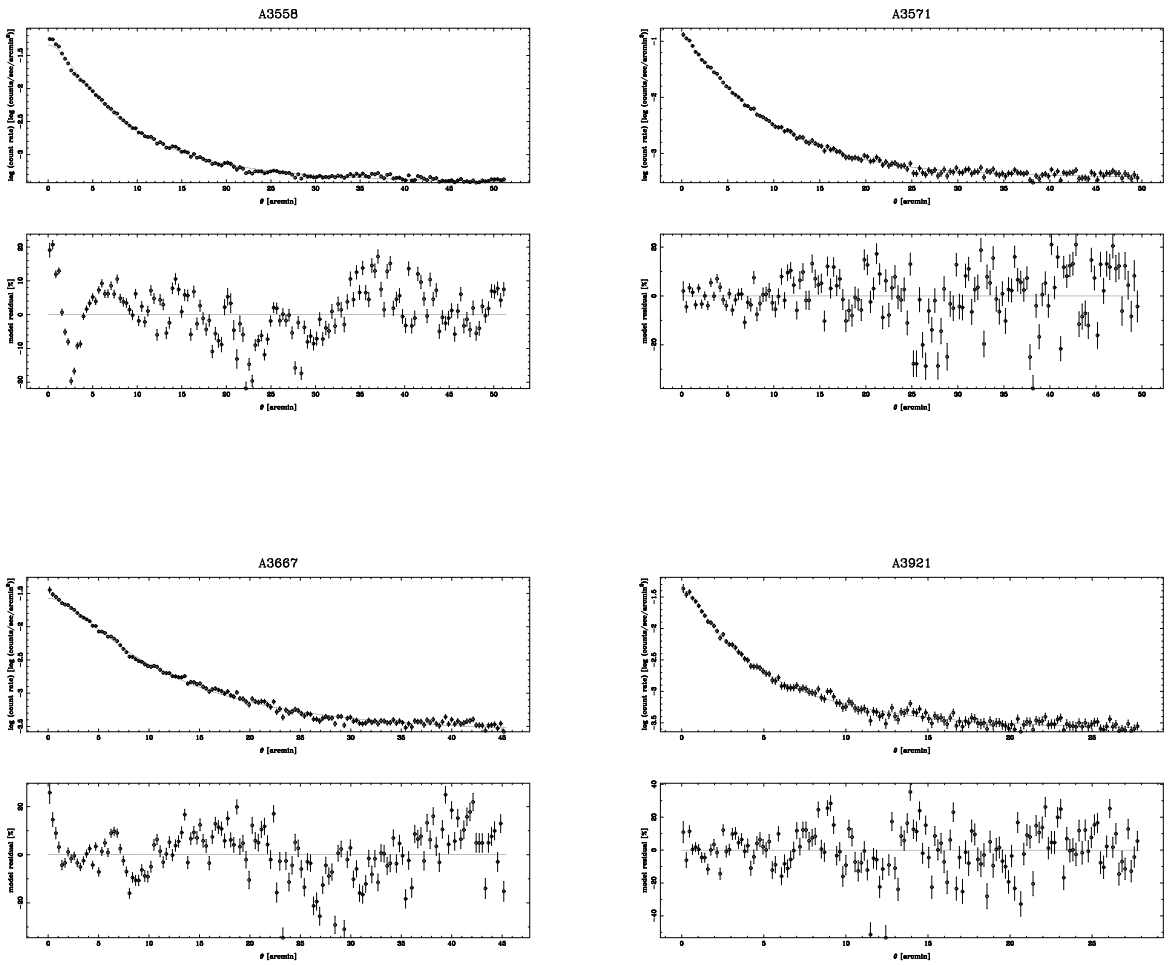


Fig. 6.— Radial profiles for A3558, A3571, A3667, A3921. The x-axis is in units of arcminutes and the y-axis the log of the azimuthally averaged count rate in units of  $\text{counts/sec/arcmin}^2$ .

## REFERENCES

- Abell, G. O. 1958, *Astrophys. J. Suppl.*, 3, 211
- Abell, G. O., Corwin, H. G., J., & Olowin, R. P. 1989, *Astrophys. J. Suppl.*, 70, 1
- Allen, S. W., Fabian, A. C., Johnstone, R. M., White, D. A., Daines, S. J., Edge, A. C., & Stewart, G. C. 1993, *Mon. Not. R. Astr. Soc.*, 262, 901
- Anders, E. & Grevesse, N. 1989, *Geochimica et Cosmochimica Acta*, 53, 197
- Bahcall, J. N. & Sarazin, C. L. 1977, *Astrophys. J. Letters*, 213, L99
- Bahcall, N. A., Ostriker, J. P., Perlmutter, S., & Steinhardt, P. J. 1999, *Science*, 284, 1481
- Briel, U. G. & Henry, J. P. 1996, *Astrophys. J.*, 472, 131
- Cavaliere, A., Danese, L., & De Zotti, G. 1979, *Astron. Astrophys.*, 75, 322
- Cavaliere, A. & Fusco-Femiano, R. 1976, *Astrophys. J.*, 49, 137
- Challinor, A. & Lasenby, A. 1998, *Astrophys. J.*, 499, 1
- Daisuke, N., Sulkanen, M. E., & Evrard, A. E. 1999, *Mon. Not. R. Astr. Soc.*, submitted
- Dalton, G. B., Efstathiou, G., Maddox, S. J., & Sutherland, W. J. 1994, *Mon. Not. R. Astr. Soc.*, 269, 151
- David, L. P., Slyz, A., Jones, C., Forman, W., Vrtilik, S. D., & Arnaud, K. A. 1993, *Astrophys. J.*, 412, 479
- Ebeling, H., Voges, W., Bohringer, H., Edge, A. C., Huchra, J. P., & Briel, U. G. 1996, *Mon. Not. R. Astr. Soc.*, 281, 799
- Edge, A. C., Stewart, G. C., Fabian, A. C., & Arnaud, K. A. 1990, *Mon. Not. R. Astr. Soc.*, 245, 559
- Evrard, A. E., Metzler, C. A., & Navarro, J. F. 1996, *Astrophys. J.*, 469, 494



- Fabricant, D., Beers, T. C., Geller, M. J., Gorenstein, P., Huchra, J. P., & Kurtz, M. J. 1986, *Astrophys. J.*, 308, 530
- Giacconi, R., Murray, S., Gursky, H., Kellogg, E., Schreier, E., & Tananbaum, H. 1972, *Astrophys. J.*, 178, 281
- Grego, L. 1998, PhD thesis, California Institute of Technology, Pasadena, CA
- Gunn, K. F. & Thomas, P. A. 1996, *Mon. Not. R. Astr. Soc.*, 281, 1133
- Henriksen, M. J. & Markevitch, M. L. 1996, *Astrophys. J. Letters*, 466, L79
- Henry, J. P. & Briel, U. G. 1995, *Astrophys. J. Letters*, 443, L9
- . 1996, *Astrophys. J.*, 472, 137
- Herbig, T., Lawrence, C. R., Readhead, A. C. S., & Gulkis, S. 1995, *Astrophys. J. Letters*, 449, L5
- Holzappel, W. L., Arnaud, M., Ade, P. A. R., Church, S. E., Fischer, M. L., Mauskopf, P. D., Rephaeli, Y., Wilbanks, T. M., & Lange, A. E. 1997, *Astrophys. J.*, 480, 449
- Hughes, J. P., Gorenstein, P., & Fabricant, D. 1988a, *Astrophys. J.*, 329, 82
- Hughes, J. P., Yamashita, K., Okumura, Y., Tsunemi, H., & Matsuoka, M. 1988b, *Astrophys. J.*, 327, 615
- Irwin, J. A., Bregman, J. N., & Evrard, A. E. 1999, *Astrophys. J.*, in press
- Iwasawa, K., Fabian, A. C., & Nandra, K. 1999, *Mon. Not. R. Astr. Soc.*, 307, 611
- Leitch, E. 1998, PhD thesis, California Inst. of Tech., Pasadena, CA.
- Markevitch, M., Forman, W. R., Sarazin, C. L., & Vikhlinin, A. 1998, *Astrophys. J.*, 503, 77
- Markevitch, M. & Vikhlinin, A. 1997, *Astrophys. J.*, 474, 84
- Mason, B. 1999, PhD thesis, University of Pennsylvania, Philadelphia, PA

- Mathiesen, B., Evrard, A. E., & Mohr, J. J. 1999, *Astrophys. J. Letters*, 520, L21
- Mitchell, R. J., Culhane, J. L., Davison, P. J. N., & Ives, J. C. 1976, *Mon. Not. R. Astr. Soc.*, 175, 29P
- Mohr, J. J., Mathiesen, B., & Evrard, A. E. 1999, *Astrophys. J.*, in press, astro-ph/9901281
- Myers, S. T., Baker, J. E., Readhead, A. C. S., Leitch, E. M., & Herbig, T. 1997, *Astrophys. J.*, 485, 1
- Navarro, J. F., Frenk, C. S., & White, S. D. M. 1997, *Astrophys. J.*, 490, 493
- Peres, C. B., Fabian, A. C., Edge, A. C., Allen, S. W., Johnstone, R. M., & White, D. A. 1998, *Mon. Not. R. Astr. Soc.*, 298, 416
- Press, W. H., Teukolsky, S. A., Vetterling, W. T., & Flannery, B. P. 1992, *Numerical recipes in C. The art of scientific computing* 2nd ed. (Cambridge: Cambridge University Press)
- Rephaeli, Y. 1995, *Astrophys. J.*, 445, 33
- Rybicki, G. B. & Lightman, A. P. 1979, *Radiative processes in astrophysics* (New York: Wiley-Interscience)
- Sazonov, S. Y. & Sunyaev, R. A. 1998, *Astrophys. J.*, 508, 1
- Scaramella, R., Zamorani, G., Vettolani, G., & Chincarini, G. 1991, *Astron. J.*, 101, 342
- Snowden, S. L., Freyberg, M. J., Plucinsky, P. P., Schmitt, J. H. M. M., Truemper, J., Voges, W., Edgar, R. J., M<sup>c</sup>Cammon, D., & Sanders, W. T. 1995, *Astrophys. J.*, 454, 643
- Snowden, S. L., M<sup>c</sup>Cammon, D., Burrows, D. N., & Mendenhall, J. A. 1994, *Astrophys. J.*, 424, 714
- Sodre, L., J., Capelato, H. V., Steiner, J. E., Proust, D., & Mazure, A. 1992, *Mon. Not. R. Astr. Soc.*, 259, 233

- Stark, A. A., Gammie, C. F., Wilson, R. W., Bally, J., Linke, R. A., Heiles, C., & Hurwitz, M. 1992, *Astrophys. J. Suppl.*, 79, 77
- Struble, M. F. & Rood, H. J. 1991, *Astrophys. J. Suppl.*, 77, 363
- Sunyaev, R. A. & Zeldovich, I. B. 1980, *Mon. Not. R. Astr. Soc.*, 190, 413
- Van Haarlem, M. P., Frenk, C. S., & White, S. D. M. 1997, *Mon. Not. R. Astr. Soc.*, 287, 817
- Vettolani, G., Chincarini, G., Scaramella, R., & Zamorani, G. 1990, *Astron. J.*, 99, 1709
- Vikhlinin, A., Forman, W., & Jones, C. 1999, *Astrophys. J.*, in press
- Weinberg, S. 1972, *Gravitation and cosmology: Principles and applications of the general theory of relativity* (New York: Wiley)
- White, D. A. & Fabian, A. C. 1995, *Mon. Not. R. Astr. Soc.*, 273, 72
- White, D. A., Jones, C., & Forman, W. 1997, *Mon. Not. R. Astr. Soc.*, 292, 419
- White, S., Navarro, J., Evrard, A., & Frenk, C. 1993, *Nature*, 366, 429